iScience

Article

BMAL1-depletion remodels ceramide metabolism to regulate ferroptosis and sorafenib chemosensitivity in acute myeloid leukemia

Graphical abstract

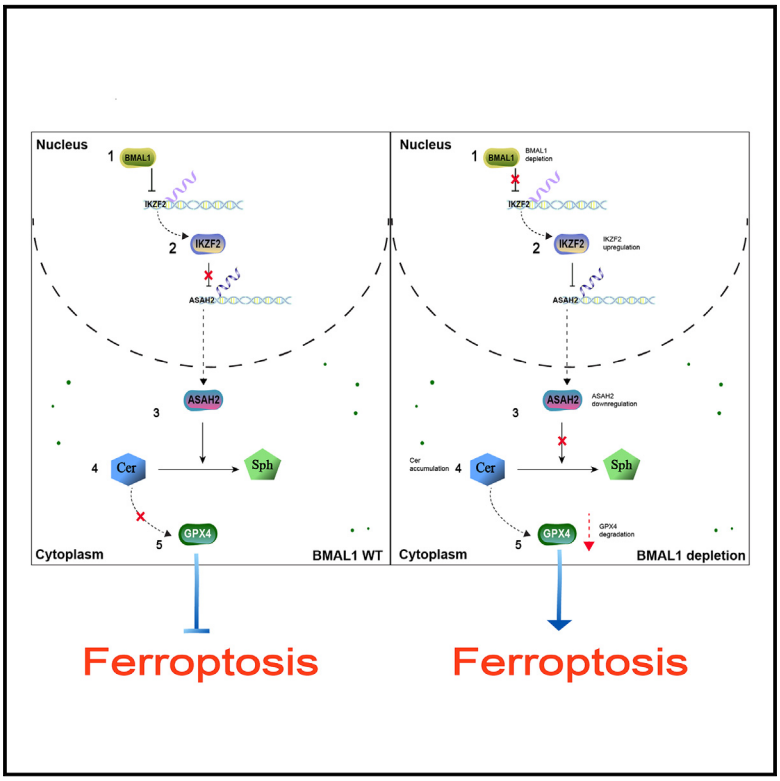

Highlights

- BMAL1 expression is downregulated in AML remission and upregulated in relapse
- BMAL1 suppresses ferroptosis in AML, promoting tumor growth and disease progression
- BMAL1 depletion induces ferroptosis in AML via ceramide accumulation
- Targeting BMAL1 or ceramide metabolism enhances AML cell response to sorafenib

Authors

Hong Zheng, Zhi Lin, Dan Wang, ..., Jie Shen, Jia-Da Li, Minghua Yang

Correspondence

lijiada@sklmg.edu.cn (J.-D.L.), yangminghua@csu.edu.cn (M.Y.)

In brief

Molecular biology; Cell biology; Cancer; Lipidomics

Zheng et al., 2025, iScience *28*, 112054
April 18, 2025
https://doi.org/10.1016/j.isci.2025.112054

CellPress

iScience

CellPress
OPEN ACCESS

Article

BMAL1-depletion remodels ceramide metabolism to regulate ferroptosis and sorafenib chemosensitivity in acute myeloid leukemia

Hong Zheng,[1,2,3,5] Zhi Lin,[1,3,5] Dan Wang,[1,3,5] Jing Zhang,[4] Ting Zeng,[1,2,3,5] Jie Shen,[1,3,5] Jia-Da Li,[4,*] and Minghua Yang[1,3,5,6,*]

[1]Department of Pediatrics, The Third Xiangya Hospital, Central South University, Changsha, Hunan 410013, China
[2]Department of Pediatrics, The Xiangya Hospital, Central South University, Changsha, Hunan 410008, China
[3]Hunan Clinical Research Center of Pediatric Cancer, The Third Xiangya Hospital, Central South University, Changsha, Hunan 410013, China
[4]Center for Medical Genetics, School of Life Sciences, Central South University, Changsha, Hunan 410008, China
[5]MOE Key Lab of Rare Pediatric Diseases, The Third Xiangya Hospital, Central South University, Changsha, Hunan 410013, China
[6]Lead contact
*Correspondence: lijiada@sklmg.edu.cn (J.-D.L.), yangminghua@csu.edu.cn (M.Y.)
https://doi.org/10.1016/j.isci.2025.112054

SUMMARY

Acute myeloid leukemia (AML) is a hematologic malignancy with a poor prognosis. We discovered that BMAL1 is a ferroptosis suppressor. Furthermore, it was also found to be overexpressed in AML patients, affecting the cell cycle and promoting tumor cell growth and progression. In this study, we further validated the association of BMAL1 with the progression and survival outcomes of AML. Lipidomic revealed that the levels of ceramide increased in AML cells following the depletion of BMAL1. Ceramide facilitated ferroptosis in AML cells. ASAH2 played a key role in this process. BMAL1 could not directly regulate ASAH2 but instead through IKZF2. Elevated levels of ceramide promoted the degradation of the ferroptosis protection molecule GPX4, ultimately promoting ferroptosis. Furthermore, ceramide treatment has been demonstrated to enhance the responsiveness of AML cells to sorafenib. In summary, this study elucidates that BMAL1 depletion remodels ceramide metabolism to regulate the sensitivity of AML cells to ferroptosis and targeted drug sorafenib.

INTRODUCTION

AML is a malignant clonal disorder distinguished by the uncontrolled growth of primitive bone marrow cells. The prognosis for AML is rather unfavorable, as the 5-year survival rate stands at a mere 30%.[1] The global annual mortality rate of AML exceeds 80,000 cases, and it is projected to double in the next twenty years.[2] Currently, chemotherapy serves as the mainstay of AML treatment. Nonetheless, AML management faces formidable obstacles in the form of drug resistance and relapse, presenting significant challenges. Ferroptosis is an intricately controlled mechanism of cellular death that is different from apoptosis.[3] Tumor cells display a remarkable sensitivity toward ferroptosis.[4] Consequently, the intentional induction of ferroptosis in cancer cells has become a compelling avenue for therapeutic intervention.

Ferroptosis is marked by a dysregulation in the intracellular oxidative-antioxidative equilibrium, leading to the propagation of lipid peroxidation. The regulation of ferroptosis involves the participation of a variety of transcription factors. NFE2L2, HIF1A, HSF1, and BMAL1 exert their regulatory function by orchestrating the activation of antioxidant genes, thereby safeguarding cells against the initiation of ferroptosis.[5] GPX4, an essential antioxidant molecule, serves as a pivotal anti-ferroptosis protein.[6] Given the widespread expression of GPX4 in most tumor cells and its critical role in sustaining their survival, targeting GPX4 emerges as a paramount strategy for inducing ferroptosis in tumors.[7] Accumulated scientific research has provided compelling findings that highlight the effectiveness of suppressing GPX4 activity to induce ferroptosis as a promising strategy for overcoming drug resistance to agents such as temozolomide, cisplatin, cetuximab, sunitinib.[8–11] In our previous study, we demonstrated that BMAL1 functions as a suppressor of ferroptosis.[12] Additionally, the study findings demonstrate that leukemia stem cell proliferation and maintenance are dependent on BMAL1, in contrast to normal cells.[13] What is more, significant progress has been made in harnessing the potential of BMAL1 as a target for therapeutic strategies in the treatment of solid tumors.[14–16] Therefore, targeting BMAL1 represents an effective strategy for exploring novel treatment strategies for AML.

Dysregulation of lipid metabolism represents a critical event in the process of ferroptosis. Sphingolipids are a significant constituent of lipids. Recently, a growing body of research has implicated abnormalities in sphingolipid pathways in a multitude of diseases, with numerous therapeutic agents targeting sphingolipids.[17,18] Notably, sphingolipid pathways are also intricately linked to tumorigenesis.[19] The intricate connection between sphingolipid metabolism and the survival and death of tumor cells exerts a profound

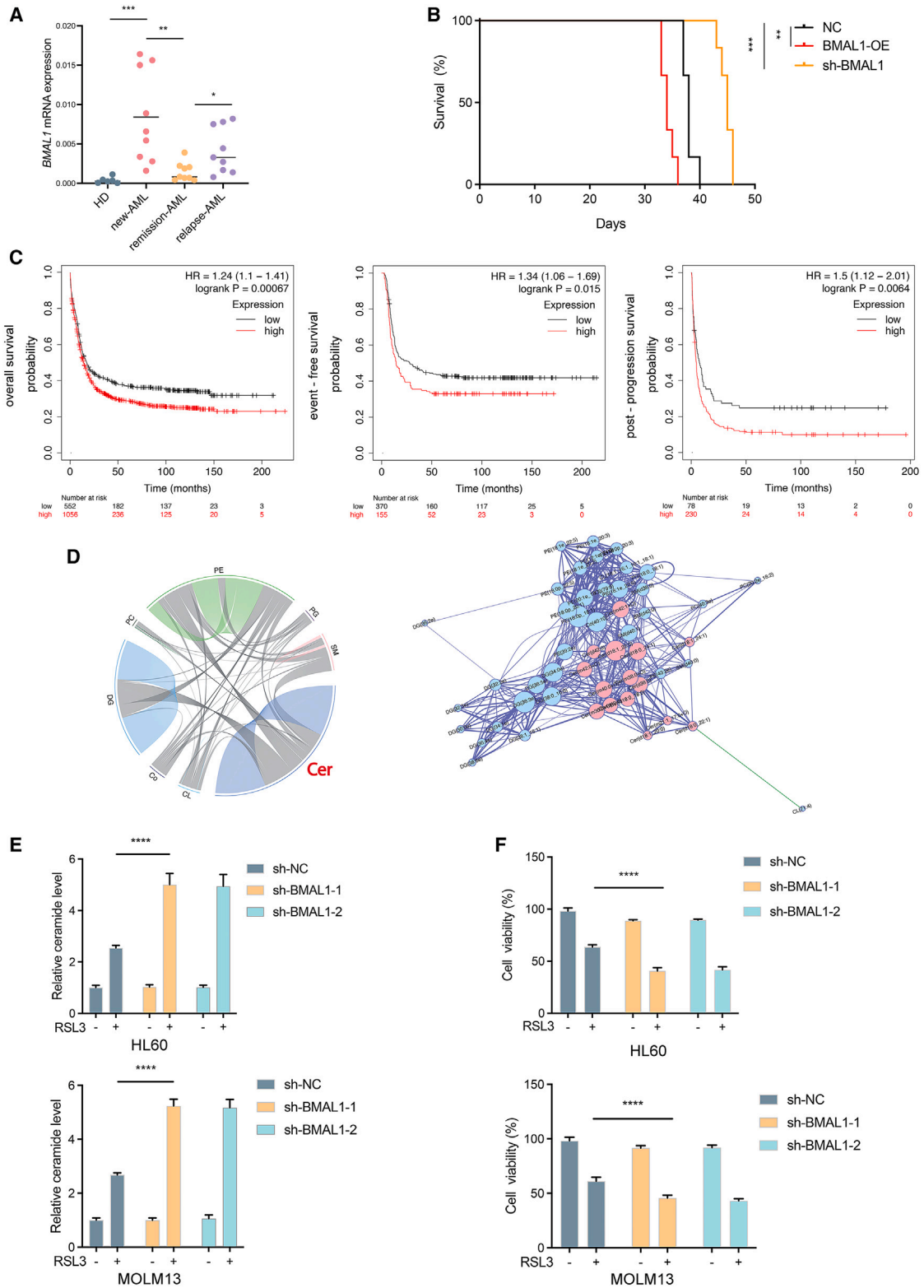

Figure 1. BMAL1-deletion upregulates ceramide level in AML cells

(A) qPCR validation of BMAL1 expression in peripheral blood mononuclear cells from healthy donors (HD [*n* = 6])and bone marrow cells from newly diagnosed (*n* = 9), remission (*n* = 9), and relapse (*n* = 9) stage AML patients.

(legend continued on next page)

influence on the course of the disease and the effectiveness of therapeutic interventions.[20] Ceramide, a key component of sphingolipids, operates as a potent signaling molecule in a variety of cellular activities, encompassing cell proliferation, differentiation, and programmed cell death. Cellular stress triggers an increase in ceramide levels, thereby promoting tumor cell death through autophagy,[21,22] apoptosis,[23] and necrotic apoptosis.[24] Conversely, tumor cells evade cellular death by reducing ceramide levels.[25,26] In recent years, there has been growing interest in leveraging cellular ceramide levels as a potential therapeutic strategy for the treatment of AML.[27] Targeting ceramide metabolism-related enzymes, including sphingosine kinases (SPHKs),[28,29] acid ceramidase (AC)[30] and glucosylceramide synthase (GCS)[31,32] have been explored. However, the role of ceramide and its metabolism in ferroptosis remains uncertain.

This study unveils fresh perspectives on the regulatory mechanism employed by the ferroptosis suppressor protein BMAL1 in AML cells. High expression of BMAL1 in AML patients correlates with poor prognosis. Targeted suppression of BMAL1 through the IKZF2-ASAH2 pathway reshapes ceramide metabolism, promoting ferroptosis in AML cells. Significantly, inhibiting BMAL1 enhances AML cell sensitivity to the anticancer drug sorafenib. In conclusion, this study unravels the mechanistic involvement of ceramide metabolism in ferroptosis of AML cells and highlights the potential of combining BMAL1 inhibitors with ceramide/sorafenib to enhance ferroptosis in AML cells. Exploring clinically applicable BMAL1 inhibitors is a direction and focal point for future research.

RESULTS

BMAL1-deletion upregulates ceramide level in AML cells

In our previous study, we found that BMAL1 was overexpressed in AML, promoting the proliferation of AML cells and tumor growth.[33] Further analysis of clinical samples revealed that BMAL1 was downregulated in AML patients who achieved remission compared to newly diagnosed AML patients, while its expression was upregulated in relapsed AML patients (Figure 1A). Correlation analysis revealed a significant association between BMAL1 expression and the proportion of $CD34^+$ cells in patients (Spearman r = 0.83, $p < 0.0001$) (Table S1). The clinical information of the participants can be found in Table S2. Based on these findings, we then established mice tumor model by intravenous injection of AML cells. The survival curve results suggested that high BMAL1 expression shortened the survival time of the mice, while knocking down BMAL1 had the opposite effect (Figures 1B and S1A). The Cancer Genome Atlas (TCGA) data analysis also indicated that BMAL1 was overexpressed in AML patients and was associated with shortened overall survival, event-free survival, and progression-free survival (Figures 1C and S1B). Furthermore, our previous investigations have unveiled the suppressive role of BMAL1 for ferroptosis under condition induced by RSL3, but not by erastin.[12] Therefore, the suppression of BMAL1 to induce ferroptosis in leukemia cells emerges as a potent therapeutic approach for addressing AML.

Lipid peroxidation serves as a crucial process in the initiation and progression of ferroptosis.[3] Recognizing the significance of lipid metabolism for ferroptosis, the underlying mechanism by which BMAL1 may regulate lipid metabolism to impact ferroptosis remains undetermined. Therefore, our aim was to delve deeper into the potential impact of BMAL1 on ferroptosis by modulating lipid metabolism. First, we knocked down BMAL1 in HL60 cells using shRNA lentivirus (Figure S1A) and subsequently performed non-targeted lipidomic analysis. Through the application of rigorous screening criteria, characterized by a VIP (variable importance in projection) value exceeding 1 and a p value below 0.05, we have adeptly discerned four distinct lipid classes (ceramide [Cer], diglyceride [DG], coenzyme [Co], and hexosylceramide [Hex2Cer]) from a comprehensive pool of 3,430 lipid molecules belonging to 39 major categories (Figure S1C). In our analysis of lipid molecules with significant differences, we discovered that the ceramide class exhibited the highest number of differentially expressed lipids (Figure S1D). Subsequently, we conducted a more detailed analysis to investigate the interplay among these distinct lipid species. Notably, our results indicated that ceramide molecules occupied a central position within this lipid network (Figure 1D). A correlation between BMAL1 and the sphingolipid metabolism pathway was unveiled through analysis of TCGA data (Figure S1E). The correlation results showed a significant p value of 0.001, indicating a robust statistical association, along with a correlation coefficient of 0.27. Although the correlation coefficient was relatively weak in strength, it still denoted a relationship between BMAL1 and sphingolipid metabolism. Subsequently, we further analyzed the carbon chain length and unsaturation of ceramide. Our results showed that AML cells predominantly expressed ceramides with total carbon atom counts of 34–36, 38, and 42. Knock down of BMAL1 resulted in an upward trend in the expression of ceramides with these total carbon atom counts, although the difference was not statistically significant (Figure S1F). Additionally, our analysis revealed that AML cells mainly expressed ceramides

(B) Kaplan-Meier curves of control, BMAL1-OE or BMAL1 shRNA HL60 AML tumor-bearing mice (n = 6 mice/group).
(C) Kaplan-Meier curve indicating overall survival, event free survival and post progression survival of patients based on AML BMAL1 expression from TCGA database. AML patients were categorized into high-BMAL1 and low-BMAL1 mRNA expression groups utilizing the minimum p value approach.
(D) Lipid-lipid interaction networks. Lipid molecule pairs with a correlation coefficient of $|r|>0.8$ and $p < 0.05$. Chord diagram (left), the points of the inner circle links represent significantly different lipid molecules, while the outer circle arcs represent lipid subclasses. Colored lines depict the correlation among lipid molecules within the subclasses. Dark gray lines represent the correlation between different subclasses. Network diagram (right), the nodes represent significantly different lipid molecules, with larger nodes indicate higher degrees. The color of the lines represents the correlation, where purple indicates positive correlation and green indicates negative correlation. Thicker lines represent stronger correlations.
(E and F) The level of ceramide and viability analysis of HL60 and MOLM13 cells with control or BMAL1 shRNA (versus blank control group). Cells were treated with or without RSL3 (0.5 μM) for 24 h. Data are presented as mean ± SD, n = 3 biologically independent samples.
Statistical tests used: (A), Mann-Whitney U test. (B and C), log rank test p values are shown. (E and F), two-way ANOVA using Dunnett multiple comparisons test with adjusted p values are shown. *$p < 0.05$, **$p < 0.01$, ***$p < 0.001$, and ****$p < 0.0001$.

with 0–2 degrees of unsaturation. Knockdown of BMAL1 also led to an increasing trend in these ceramides, but it was also not statistically significant (Figure S1G). As a result, our subsequent research did not specifically concentrate on any particular subclass of ceramide, but rather on the overall levels of ceramide. What's more, studies have provided evidence linking ceramide to tumor progression.[34,35] However, the intricate relationship between ceramide and the induction of ferroptosis in AML cells continues to baffle researchers. To further validate the influence of BMAL1 on ceramide levels, we conducted ELISA experiments to measure changes in ceramide levels. Our investigation revealed a compelling association between the upregulation of BMAL1 and a significant reduction in ceramide levels, resulting in a notable decrease in cell death within HL60 and MOLM13 cells under RSL3-induced ferroptosis condition (Figures S1H and S1I). In contract, the downregulation of BMAL1 led to an observable increase in ceramide levels and a consequential rise in cell death in the presence of RSL3-induced ferroptosis (Figures 1E and 1F). It is noteworthy that, under non-ferroptotic conditions, there were no significant changes observed in ceramide levels and cell death after either overexpressing or knocking down BMAL1 (Figures 1E, 1F, S1H, and S1I). Based on these comprehensive results, we propose that under conditions of RSL3-induced ferroptosis, BMAL1-deletion sensitizes AML cell to ferroptosis by upregulating ceramide levels.

Ceramide upregulation sensitizes AML cells to lipid peroxidation and ferroptosis

In order to explore the potential contribution of ceramide to the regulatory role of BMAL1 in ferroptosis of AML cells, we conducted a comprehensive analysis to examine how alterations in ceramide levels impact the occurrence of ferroptosis in AML cells. After determining a non-cytotoxic concentration of C2-ceramide that did not affect AML cell viability (Figures S2A–S2C), we performed exogenous C2-ceramide addition experiments at a concentration of 5 μM. Through the inclusion of exogenous C2-ceramide and the subsequent evaluation of its effects on AML cells, we discovered that the supplementation of C2-ceramide facilitated cell death, malondialdehyde (MDA) generation, and lipid peroxidation (Figures 2A–2C). The aforementioned results were all reversed by ferrostain-1 (a ferroptosis inhibitor) (Figures 2A–2C). Simultaneously, overexpressing BMAL1 reduced the C2-ceramide-promoted cell death, MDA production, and lipid peroxidation (Figures 2A–2C). Conversely, when we inhibited *de novo* ceramide synthesis using myriocin (ISP-1), we observed a reversal of the promotion of cell death induced by BMAL1 knockdown, as well as a suppression of MDA generation and lipid peroxidation (Figures 2D–2F). To summarize, these collective findings underscore the crucial role of BMAL1 in exerting regulatory control over the ferroptosis in AML cells via modulating ceramide levels.

ASAH2 is the key mediator in the elevation of ceramide levels induced by BMAL1 knockdown

Subsequently, we delved into elucidating the underlying mechanism of BMAL1 knockdown-induced elevation of ceramide levels during RSL3-induced ferroptosis in AML cells. Through comprehensive KEGG (Kyoto Encyclopedia of Genes and Genomes) pathway analysis, we meticulously identified the crucial enzymes involved in ceramide metabolism (Figure 3A). We examined the expression trends of these ceramide metabolism genes in HL60 and MOLM13 cells after either overexpressing or knocking down BMAL1. Our results revealed that only the ASAH2 gene exhibited opposite and statistically significant expression changes following BMAL1 overexpression or knockdown (Figure 3B). ASAH2, encoding the neutral ceramidase enzyme, tightly regulates ceramide metabolism by catalyzing the conversion of ceramide into fatty acids and sphingosine. Downregulation of ASAH2 leads to ceramide accumulation. Initially, we investigated the effects of downregulating ASAH2 on ceramide levels and ferroptosis in AML cells. Our findings revealed that both ASAH2 inhibition using ceranib-1 and ASAH2 knockdown via shRNA resulted in elevated ceramide levels (Figures S3A and S3F), which facilitated cell death (Figures S3B and S3G), MDA production (Figures S3C and S3H), lipid peroxidation (Figures S3D and S3I), and GPX4 autophagic degradation (Figures S3E and S3J) in AML cells undergoing ferroptosis. Subsequently, western blot experiments confirmed that BMAL1 overexpression upregulated ASAH2 in HL60 and MOLM13 cells, while BMAL1 knockdown downregulated ASAH2 (Figures 3C and S4A). Importantly, our results indicated that the overexpression of BMAL1 followed by ASAH2 knockdown increased ceramide levels, cell death, MDA production, lipid peroxidation (Figures 3D and S4B–S4D) compared to the BMAL1 overexpression group. In conclusion, these findings suggest that BMAL1 modulates ceramide metabolism in AML cells during ferroptosis by regulating ASAH2.

IKZF2 mediates BMAL1's regulation of ASAH2

BMAL1 serves as a critical transcription factor, orchestrating the expression of multiple genes to modulate diverse cellular physiological processes.[36] In order to clarify how BMAL1 regulates ASAH2, we utilized the JASPAR database to predict the sites where BMAL1 binds to ASAH2. The JASPAR database, known for its high quality and public accessibility, is a valuable resource for predicting potential binding sites of transcription factors within target gene promoter regions. In our study, we focused on analyzing the 2k bp sequence upstream of the transcription start site of the ASAH2 gene to predict binding sites for BMAL1, with a score threshold of 80%. However, our analysis indicated the absence of BMAL1 binding sites within the promoter region of ASAH2. Furthermore, our investigation of the public chromatin immunoprecipitation (ChIP) database revealed no evidence of BMAL1's direct regulation of ASAH2. Additionally, our ChIP experiment results indicated that BMAL1 was unable to bind to the promoter of ASAH2 to directly regulate the transcription of ASAH2 (Figure 4A). In light of the aforementioned discoveries, we inferred that BMAL1 regulates ASAH2 through an intermediary molecule. Hence, we proceeded to analyze the 1,666 genes predicted to be regulated by BMAL1 and the 294 potential transcription factors for ASAH2. Remarkably, we discovered an intersection of 24 genes between the two sets (Figure 4B). Afterward, we explored how the expression of these 24 genes changed in AML cells when BMAL1 was either overexpressed or knocked down. Our results revealed that IKZF2 exhibited significant and opposite expression changes after

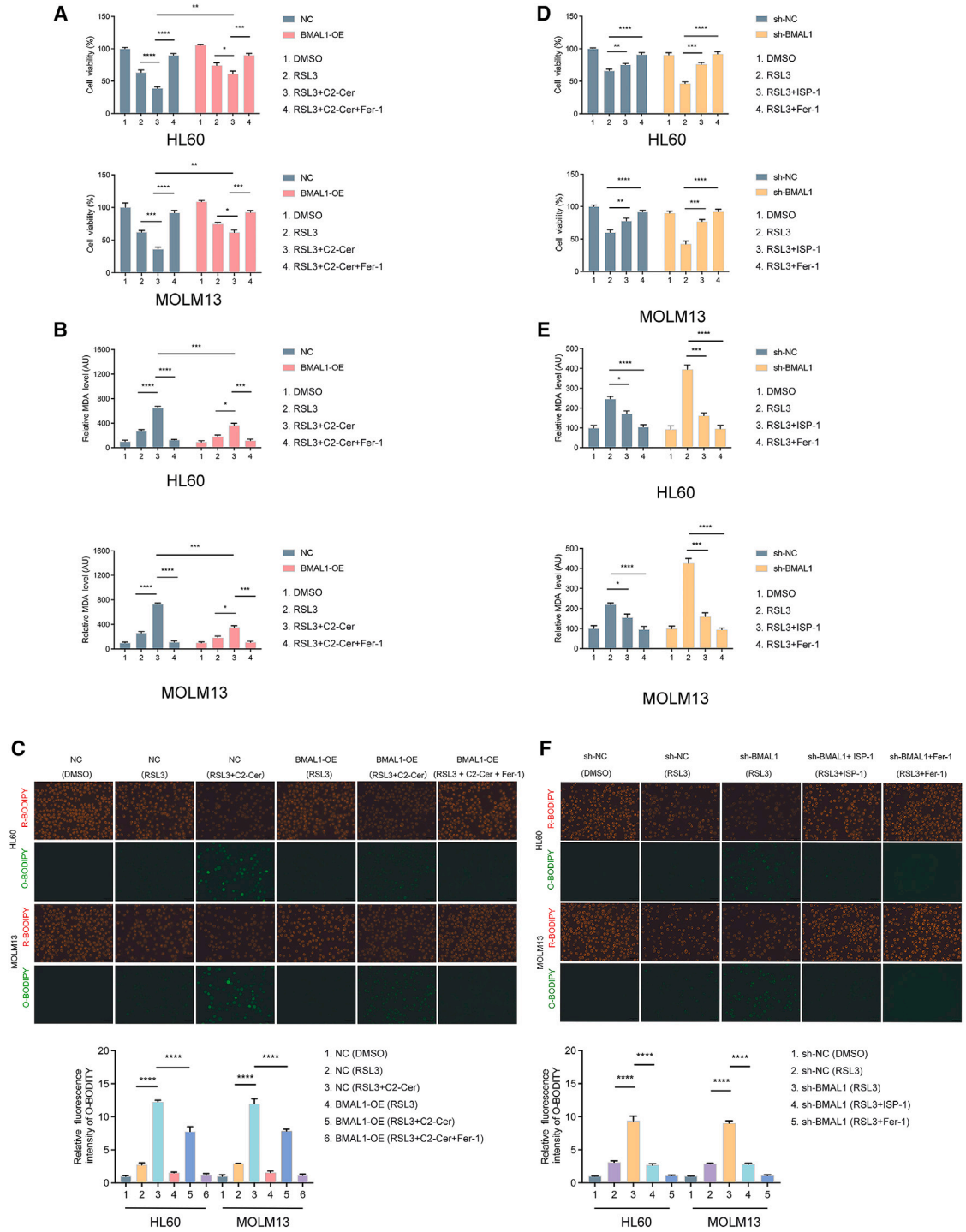

Figure 2. Ceramide upregulation sensitizes AML cells to lipid peroxidation and ferroptosis

(A–C) Viability analysis, the level of MDA and the lipid ROS of HL60 and MOLM13 cells with control or BMAL1-OE (versus blank control group). Scale bar: 100 μm. Cells were treated with RSL3 (0.5 μM) in the presence or absence of C2-ceramide (C2-Cer, 5.0 μM) or ferrostain-1 (Fer-1, 0.5 μM) for 24 h.

(D–F) Viability analysis, the level of MDA and the lipid ROS of HL60 and MOLM13 cells with control or BMAL1 shRNA (versus blank control group). Cells were treated with RSL3 (0.5 μM) in the presence or absence of myriocin (ISP-1, 1.0 μM) or ferrostain-1(Fer-1, 0.5 μM) for 24 h, Scale bar: 100 μm. Before treating with RSL3, the cells were pre-treated with ISP-1 for 24 h. Data are presented as mean ± SD, $n = 3$ biologically independent samples.

Statistical tests used: (A, B, D, and E), two-way ANOVA using Šídák multiple comparisons test with adjusted p values are shown. (C and F), one-way ANOVA using Tukey multiple comparisons test with adjusted p values are shown. *$p < 0.05$, **$p < 0.01$, ***$p < 0.001$, and ****$p < 0.0001$.

A

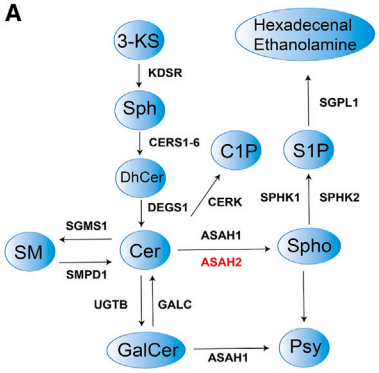

B

sphingolipid metabolic enzyme	Fold change(shBMAL1/WT)& *P* value				Fold change(BMAL1-OE/WT)& *P* value			
	HL60		MOLM13		HL60		MOLM13	
ACER1	0.93	N.S.	1.12	N.S.	0.87	N.S.	1.67	N.S.
ASAH1	0.78	*	0.834	N.S.	0.98	N.S.	0.94	N.S.
ASAH2	0.65	**	0.55	***	3.41	**	4.73	***
GALC	0.87	N.S.	1.16	N.S.	1.63	N.S.	1.46	N.S.
UGT8	1.17	N.S.	1.38	N.S.	0.94	N.S.	1.47	N.S.
CERK	0.94	N.S.	1.21	N.S.	0.88	N.S.	1.15	N.S.
SMPD1	1.56	N.S.	0.92	N.S.	0.77	N.S.	0.95	N.S.
SGMS1	1.81	N.S.	1.79	*	0.94	N.S.	0.67	**
SGPL1	1.02	N.S.	1.28	N.S.	0.91	N.S.	1.18	N.S.
SPHK1	0.64	N.S.	0.82	*	0.86	N.S.	1.98	*
SPHK2	0.82	N.S.	0.84	*	0.93	N.S.	1.88	*
KDSR	1.12	N.S.	1.02	N.S.	0.89	N.S.	0.86	N.S.
CERS1	1.01	N.S.	0.90	N.S.	0.93	N.S.	1.12	N.S.
CERS2	1.17	N.S.	1.20	N.S.	0.95	N.S.	0.78	*
CERS3	1.21	N.S.	1.09	N.S.	0.87	*	0.95	N.S.
CERS4	1.19	N.S.	1.16	N.S.	0.92	N.S.	0.93	N.S.
CERS5	1.14	N.S.	1.22	N.S.	0.91	N.S.	0.95	N.S.
CERS6	1.13	N.S.	1.24	N.S.	0.93	N.S.	0.91	N.S.
DEGS1	1.52	N.S.	1.42	N.S.	0.86	N.S.	0.88	N.S.

C

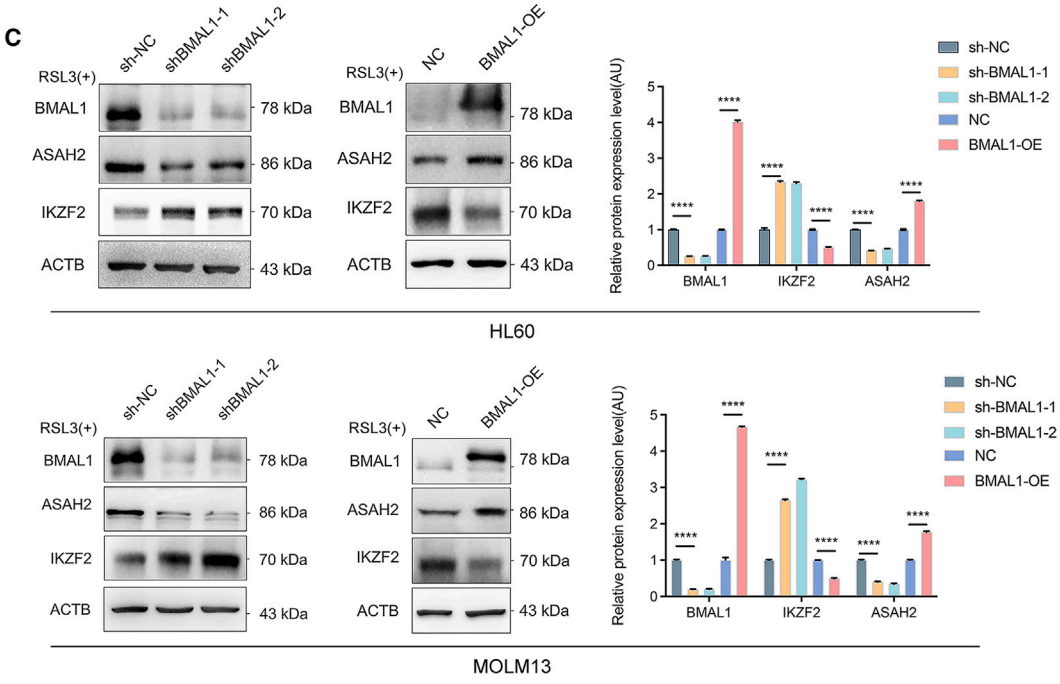

D

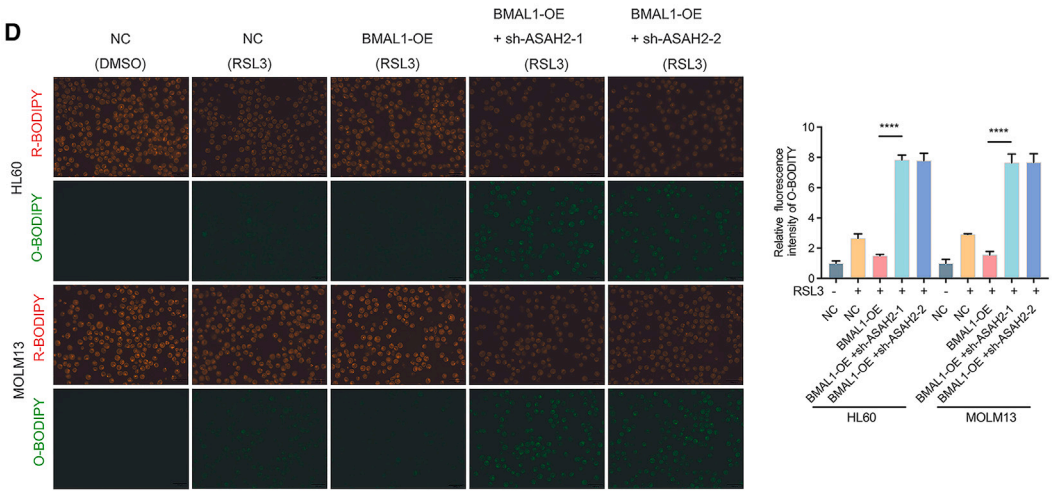

(legend on next page)

BMAL1 overexpression or knockdown (Figure 4C). Moreover, western blot analysis demonstrated that BMAL1 overexpression downregulated IKZF2 protein levels, whereas BMAL1 knockdown resulted in an increase in IKZF2 protein levels (Figures 3C and S4A).

We further conducted experiments to investigate the regulatory role of IKZF2 on ASAH2. Initially, the IKZF2 inhibitor NVP-DKY709 was utilized to assess its influence on the expression of ASAH2 and the levels of ceramide. According to our findings, the pharmacological inhibition of IKZF2 resulted in an increase in ASAH2 mRNA and protein expression, coupled with a decrease in ceramide levels in HL60 and MOLM13 cells (Figures S5A–S5C). Subsequent experiments revealed a significant decrease in ASAH2 mRNA and protein levels, alongside a concurrent increase in ceramide, when IKZF2 was overexpressed in HL60 and MOLM13 cells (Figures 4D–4F and S5D). In contrast, knocking down IKZF2 resulted in an increase in ASAH2 mRNA and protein levels, as well as a decrease in ceramide levels. (Figures 4D–4F and S5D).

To further validate the regulation of ASAH2 by BMAL1 through IKZF2, we conducted predictions of potential binding sites for BMAL1 within the IKZF2 promoter region and for IKZF2 within the ASAH2 promoter region using the JASPAR database. The predicted potential binding sites are illustrated (Figures S5E and S5F). Continuing with the ChIP experiment, the results indicated a significant increase in the binding of BMAL1 to the potential promoter sites of human IKZF2 and the binding of IKZF2 to the potential promoter sites of human ASAH2 when compared to the control group (Figures 5A, 5B, S5G, and S5H). Following that, we performed a dual-luciferase reporter gene assay. The luciferase reporter vectors carrying the full-length promoter sequences of human IKZF2 or ASAH2 were co-transfected with 293T cells. Additionally, the luciferase reporter vectors containing mutated BMAL1 binding sites within the IKZF2 promoter sequence or mutated IKZF2 binding sites within the ASAH2 promoter sequence were separately co-transfected into 293T cells. Concurrently, gradient concentrations of overexpressed BMAL1 or IKZF2 plasmids were introduced. Our findings revealed a dose-dependent suppression of reporter gene activity in cells co-transfected with luciferase reporter vectors containing intact IKZF2 or ASAH2 promoter sequences, as the concentration of overexpressed BMAL1 or IKZF2 plasmids increased (Figure 5C). Conversely, in cells harboring the IKZF2 promoter sequence with mutated BMAL1 binding sites or the ASAH2 promoter sequence with mutated IKZF2 binding sites, our results demonstrated that the activity of the reporter gene was not inhibited even with the gradual increase of BMAL1 or IKZF2 overexpression plasmids (Figure 5D). These results suggest a regulatory role of BMAL1 in ASAH2 expression through IKZF2. Subsequently, we carried out rescue experiments. When BMAL1 was overexpressed followed by overexpression of IKZF2, there was a decrease in ASAH2 mRNA and protein levels (Figures 5E and 5F), accompanied by an increase in ceramide levels (Figure 5G) under the circumstances of ferroptosis induced by RSL3. Conversely, knocking down BMAL1 followed by knocking down IKZF2 resulted in an increase in ASAH2 mRNA and protein levels (Figures S6A and S6B), coupled with a decrease in ceramide levels (Figure S6C). In brief, our results provide evidence that BMAL1 regulates ceramide metabolism through the IKZF2-ASAH2 pathway.

GPX4 degradation promotes ceramide upregulation-mediated ferroptosis

The occurrence of ferroptosis is attributed to an imbalance between cellular oxidation and antioxidant systems. GPX4, an essential cellular antioxidant, plays a crucial part in preventing ferroptosis. The process by which different drugs induce cell ferroptosis involves accelerating the degradation of GPX4.[37,38] Ceramide is closely linked to cellular autophagy.[39] Studies have demonstrated that it enhances the degradation of GPX4, thereby promoting ferroptosis.[21,40] Consequently, it is hypothesized that knocking down BMAL1 leads to elevated ceramide levels, which in turn promote the degradation of GPX4, ultimately facilitating ferroptosis in AML cells. According to our research, increased BMAL1 expression was found to inhibit GPX4 degradation (Figure 5F) without inducing significant changes at the mRNA level (Figure S7A). Conversely, BMAL1 knockdown was observed to facilitate GPX4 degradation (Figure S6B) without causing notable alterations at the mRNA level (Figure S7A). Subsequently, we investigated the influence of BMAL1 on GPX4 via the IKZF2-ASAH2 pathway. Our findings demonstrated that co-overexpression of BMAL1 and IKZF2 facilitated cellular autophagy and GPX4 degradation, while also leading to elevated levels of ceramides, increased cell death, MDA production, and enhanced lipid peroxidation (Figures 5F, 5G, 6A, S7B, and S7C). Conversely, the knock down of IKZF2 reversed the promotive effects of BMAL1 knockdown on cellular autophagy, and GPX4 degradation, ceramide levels, cell death, MDA production, and lipid peroxidation (Figures 6B, S6B, S6C, S7D, and S7E). Furthermore, we observed that overexpression of BMAL1

Figure 3. ASAH2 is the key mediator in the elevation of ceramide levels induced by BMAL1 knockdown

(A) The major metabolites and the key sphingolipid metabolic genes associated with ceramide metabolism in KEGG-based sphingolipid metabolism network. 3-KS, 3-ketosphinganine; Sph, sphinganine; DhCer, dihydroceramide; Cer, ceramide; SM, sphingomyelin; GalCer, galactosylceramide; Psy, psychosine; Spho, sphingosine; C1P, ceramide-1-phosphate; S1P, sphingosine-1-phosphate.

(B) Table shows the average fold change and statistical analysis of 19 sphingolipid metabolic gene expression between BMAL1 shRNA/BMAL1-OE and their parental WT cell lines of HL60 and MOLM13 cells. Cells were treated with RSL3 (0.5 μM) for 24 h.

(C) Western blot analysis showing indicated protein expression in HL60 and MOLM13 cells with control, BMAL1-OE, or BMAL1 shRNA. Cells were treated with RSL3 (0.5 μM) for 24 h.

(D) The lipid ROS were assayed of HL60 and MOLM13 cells with control, BMAL1-OE or BMAL1-OE+ASAH2 shRNA. Cells were treated with RSL3 (0.5 μM) for 24 h, Scale bar: 100 μm. Data are presented as mean ± SD, $n = 3$ biologically independent samples.

Statistical tests used: (B), two-way ANOVA using Šídák multiple comparisons test with adjusted p values is shown. (C), two-way ANOVA using Dunnett multiple comparisons test with adjusted p values is shown. (D), one-way ANOVA using Tukey multiple comparisons test with adjusted p values is shown. $^{*}p < 0.05$, $^{**}p < 0.01$, $^{***}p < 0.001$, and $^{****}p < 0.0001$.

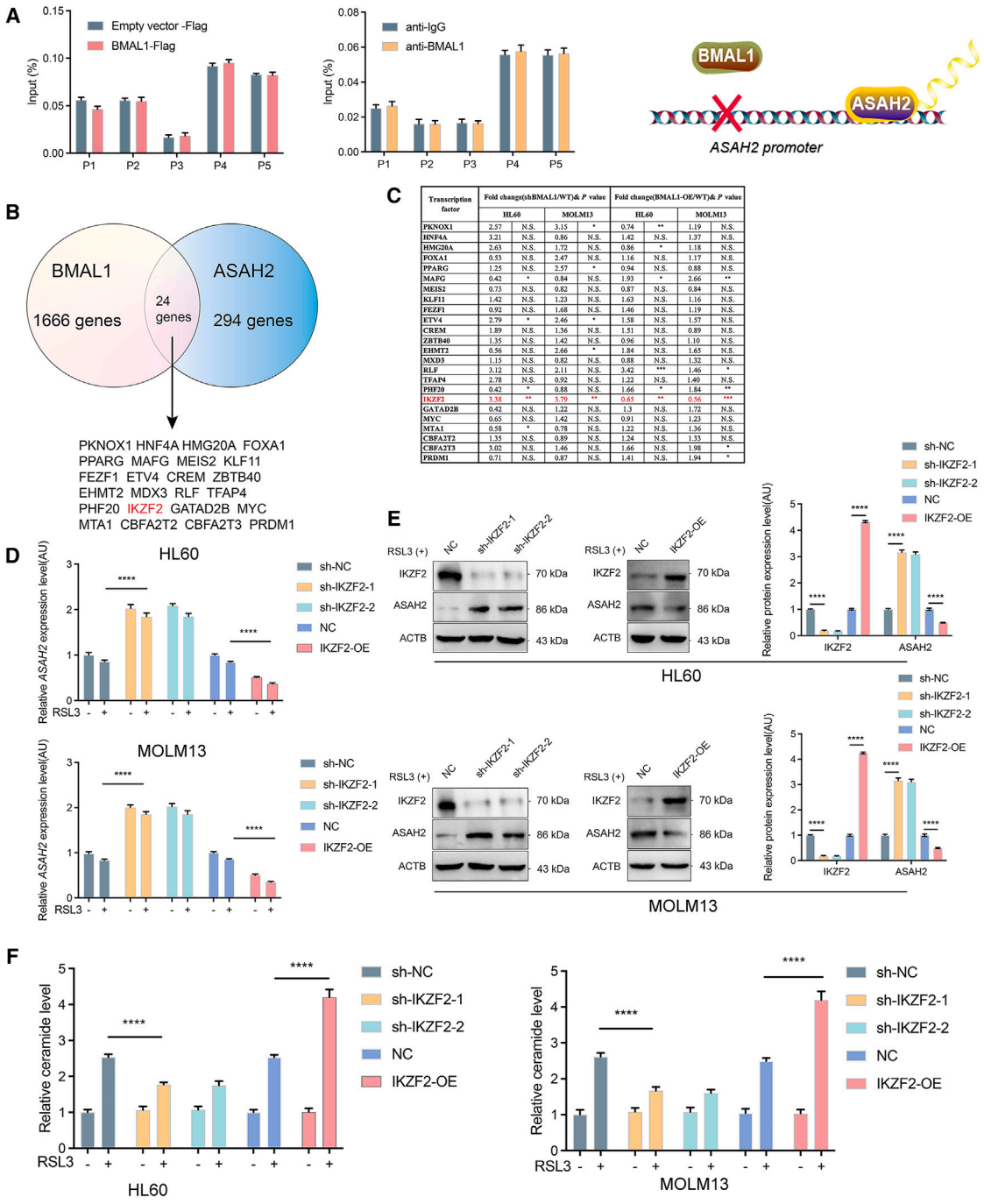

Transcription factor	Fold change(shBMAL1/WT)& *P* value				Fold change(BMAL1-OE/WT)& *P* value			
	HL60		MOLM13		HL60		MOLM13	
PKNOX1	2.57	N.S.	3.15	*	0.74	**	1.19	N.S.
HNF4A	3.21	N.S.	0.86	N.S.	1.42	N.S.	1.37	N.S.
HMG20A	2.63	N.S.	1.72	N.S.	0.86	*	1.18	N.S.
FOXA1	0.53	N.S.	2.47	N.S.	1.16	N.S.	1.17	N.S.
PPARG	1.25	N.S.	2.57	*	0.94	N.S.	0.88	N.S.
MAFG	0.42	*	0.84	N.S.	1.93	*	2.66	**
MEIS2	0.73	N.S.	0.82	N.S.	0.87	N.S.	0.84	N.S.
KLF11	1.42	N.S.	1.23	N.S.	1.63	N.S.	1.16	N.S.
FEZF1	0.92	N.S.	1.68	N.S.	1.46	N.S.	1.19	N.S.
ETV4	2.79	*	2.46	*	1.58	N.S.	1.57	N.S.
CREM	1.89	N.S.	1.36	N.S.	1.51	N.S.	0.89	N.S.
ZBTB40	1.35	N.S.	1.42	N.S.	0.96	N.S.	1.10	N.S.
EHMT2	0.56	N.S.	2.66	*	1.84	N.S.	1.65	N.S.
MXD3	1.15	N.S.	0.82	N.S.	0.88	N.S.	1.32	N.S.
RLF	3.12	N.S.	2.11	N.S.	3.42	***	1.46	*
TFAP4	2.78	N.S.	0.92	N.S.	1.22	N.S.	1.40	N.S.
PHF20	0.42	*	0.88	N.S.	1.66	*	1.84	**
IKZF2	3.38	**	3.79	**	0.65	**	0.56	***
GATAD2B	0.42	N.S.	1.22	N.S.	1.3	N.S.	1.72	N.S.
MYC	0.65	N.S.	1.42	N.S.	0.91	N.S.	1.23	N.S.
MTA1	0.58	*	0.78	N.S.	1.22	N.S.	1.36	N.S.
CBFA2T2	1.35	N.S.	0.89	N.S.	1.24	N.S.	1.33	N.S.
CBFA2T3	3.02	N.S.	1.46	N.S.	1.66	N.S.	1.98	*
PRDM1	0.71	N.S.	0.87	N.S.	1.41	N.S.	1.94	*

Figure 4. IKZF2 mediates BMAL1's regulation of ASAH2

(A) ChIP-qPCR assays were performed using anti-BMAL1, FLAG, or IgG, with primer pairs targeting the ASAH2 promoter in 293T cells.

(B) The overlap gene image of BMAL1-regulated genes and potential transcription factors of *ASAH2*.

(C) Tables show the average fold change and statistical analysis of 24 gene expression between BMAL1 shRNA/BMAL1-OE and their parental WT cell lines of HL60 and MOLM13 cells. Cells were treated with RSL3 (0.5 μM) for 24 h.

(D–F) qPCR, western blot, and the level of ceramide analysis in HL60 and MOLM13 cells with control, IKZF2-OE, or IKZF2 shRNA. Cells were treated with or without RSL3 (0.5 μM) for 24 h. Data are presented as mean ± SD, $n = 3$ biologically independent samples.

Statistical tests used: (A and C), two-way ANOVA using Šídák multiple comparisons test with adjusted *p* values are shown. (D–F), two-way ANOVA using Dunnett multiple comparisons test with adjusted *p* values are shown. $^{*}p < 0.05$, $^{**}p < 0.01$, $^{***}p < 0.001$, and $^{****}p < 0.0001$.

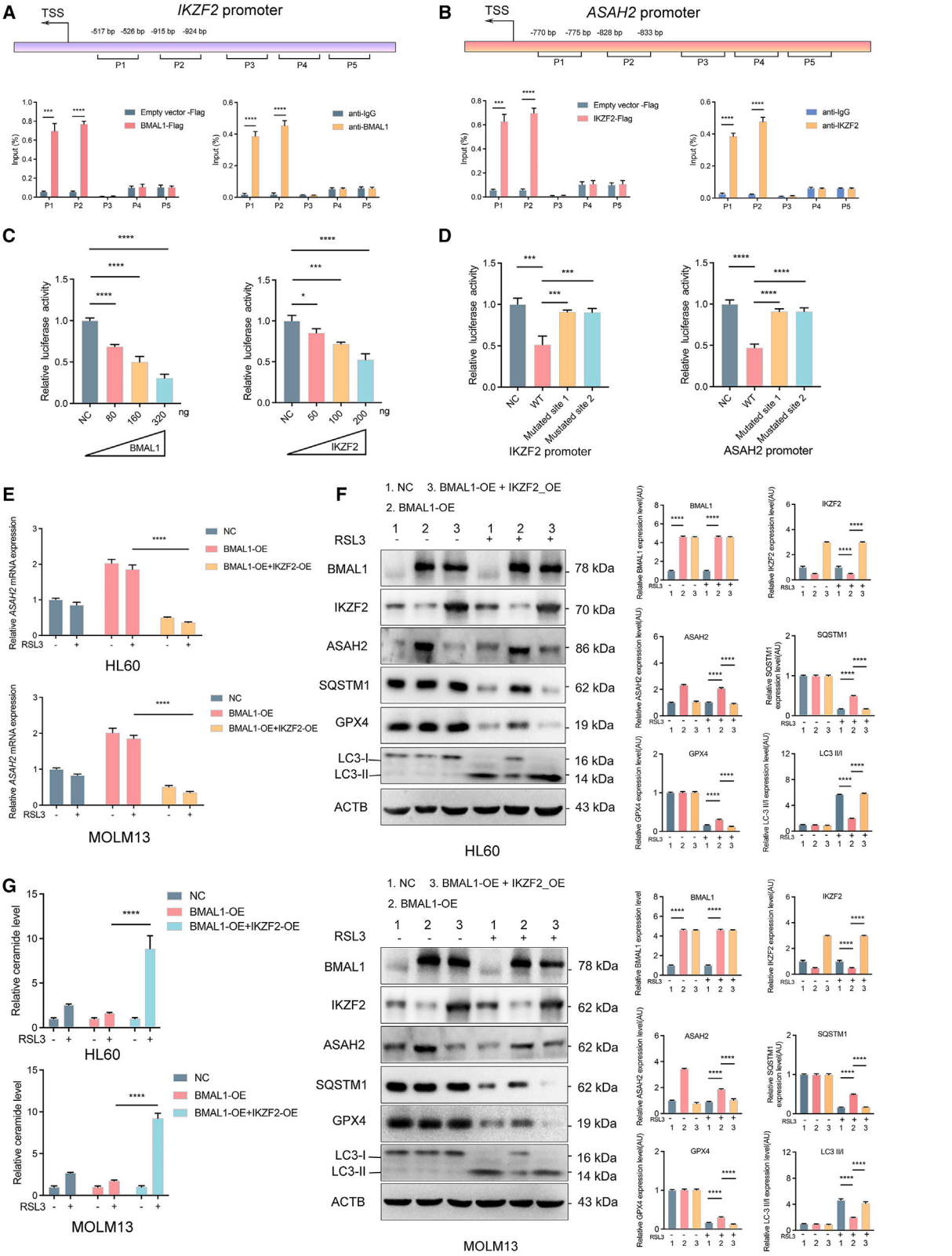

(legend on next page)

followed by ASAH2 knockdown promoted autophagy and degradation of GPX4, while also increasing levels of ceramide, cell death, MDA production, lipid peroxidation (Figures 3D, 6C, and S4B–S4D). Additionally, we observed that exogenous administration of C2-ceramide reversed the inhibitory effects of BMAL1 overexpression on cell death, MDA production, lipid peroxidation (Figures 2A–2C), autophagy and degradation of GPX4 (Figure S8A). The observed exogenous C2-ceramide addition results were effectively reversed by the administration of an autophagy inhibitor (Figures S8A and S9A–S9C). In contrast, when knocking down BMAL1, the *de novo* ceramide synthesis inhibitor myriocin could suppress cell death, MDA production, lipid peroxidation (Figures 2D–2F), cellular autophagy and GPX4 degradation (Figure S8B). To conclude, the aforementioned findings indicate that BMAL1 regulates ceramide metabolism via the IKZF2-ASAH2 pathway, subsequently influencing cellular autophagy and GPX4 degradation, thereby modulating ferroptosis in AML cells.

BMAL1 depletion boosts AML cell sensitivity to sorafenib

Then, we considered the possibility that knocking down BMAL1 might enhance the therapeutic outcomes of clinically approved drugs in the treatment of AML. The drug sorafenib, an FDA (Food and Drug Administration)-approved targeted anticancer medication, has been discovered to have dual efficacy in inducing tumor cell ferroptosis and treating AML.[41] Clinical trials (NCT03247088, NCT05596968, and NCT03132454) are currently underway to evaluate the use of sorafenib in refractory AML. Optimizing the strategy of targeting ferroptosis can significantly enhance the therapeutic response of tumors, particularly those resistant to sorafenib.[42] Consequently, based on our previous findings, we hypothesize that BMAL1 knockdown may enhance the anti-AML efficacy of sorafenib.

Our observations indicated that reducing BMAL1 levels increases the sensitivity of AML cells to sorafenib (Figure S10A). On the other hand, elevating BMAL1 expression reduces the sensitivity of AML cells to sorafenib (Figure S10B). Furthermore, it was observed that the exogenous supplementation of C2-ceramide led to an increase in cellular death, MDA production, and lipid peroxidation (Figures S11A–S11C). Notably, these effects were effectively reversed upon administration of hydroxychloroquine or ferrostain-1 (Figures S10C and S11A–S11C). Additionally, the application of ceramide *de novo* synthesis inhibitor myriocin or ferrostain-1 demonstrated a significant reduction in cell death, MDA production, and lipid peroxidation (Figures 7A, S11D, and S11E) induced by BMAL1 knockdown.

Afterward, we validated the role of the IKZF2-ASAH2 pathway in BMAL1-mediated enhancement of AML cells sensitivity to sorafenib. Our experiments revealed that overexpressing IKZF2 elevates ceramide levels and counteracts the cell death inhibition caused by BMAL1 overexpression in the context of RSL3-induced ferroptosis (Figures S10D and S10E). In contrast, knocking down IKZF2 reduces ceramide levels and reverses the cell death promotion induced by BMAL1 knockdown (Figures 7B and 7C). Furthermore, knocking down ASAH2 increases ceramide levels and reverses the cell death inhibition caused by BMAL1 overexpression in the condition of RSL3-induced ferroptosis (Figures 7D and 7E). In summary, our results indicate that the downregulation of BMAL1 enhances the sensitivity of AML cells to sorafenib by upregulating ceramide levels through the IKZF2-ASAH2 pathway. The use of BMAL1 inhibitors or ceramide significantly enhances the therapeutic effectiveness of sorafenib in the treatment of AML, and further research is needed to fully understand its clinical implications.

The BMAL1-IKZF2-ASAH2 pathway enhancing ferroptosis-mediated AML suppression *in vivo*

After that, we assessed the anti-AML effects of inhibiting the BMAL1 under RSL3-induced ferroptosis conditions via the IKZF2-ASAH2 pathway *in vivo* (Figure 8A). The AML tumor model was established by intravenously injecting HL60 cells (2×10^6/mice) into male nude mice aged 6–8 weeks. One week after the intravenous injection of tumor cells into the tail vein, the mice were evaluated for tumor modeling. Subsequently, mice meeting the modeling criteria were randomly grouped. Treatment was administered to the mice through intraperitoneal. The dose of RSL3 was 30 mg/kg, given every other day for a duration of 2 weeks. Our experimental findings revealed that overexpressing BMAL1 led to a downregulation of 4-HNE, MDA, *PTGS2* and HMGB1 (markers of ferroptosis), along with a decrease in ceramide levels (Figures 8B–8F and S12A–S12E). Mice with overexpression of BMAL1 were observed to exhibit a higher tumor burden, along with pronounced hepatosplenomegaly (Figures 8G–8J and S12F–S12I). In contrast, the knockdown of BMAL1 was observed to promote ferroptosis, characterized by elevated ceramide levels; increased levels of 4-HNE, MDA, and HMGB1; upregulation of PTGS2 mRNA; reduced hepatosplenomegaly in mice; and alleviated tumor burden (Figures 8B–8J and S12A–S12I). Additionally,

Figure 5. IKZF2 mediates BMAL1's regulation of ASAH2

(A) ChIP-qPCR assays were performed using anti-BMAL1, FLAG, or IgG, with primer pairs targeting the IKZF2 promoter in 293T cells.

(B) ChIP-qPCR assays were performed using anti-IKZF2, FLAG, or IgG, with primer pairs targeting the ASAH2 promoter in 293T cells.

(C) Luciferase assays of 293T cells co-transfected with a luciferase reporter containing a full-length human IKZF2 (left) or ASAH2 (right) promoter sequence and an escalating amount of BMAL1 (left) or IKZF2 (right) overexpression plasmid.

(D) Luciferase assays were performed on 293T cells co-transfected with a luciferase vector carrying either a full-length WT IKZF2 (left) or ASAH2 (right) promoter sequence, or a promoter sequence containing a mutated proximal or distal BMAL1 (left) or IKZF2 (right) binding site, together with 160 ng of BMAL1 (left) or 200 ng of IKZF2 (right) overexpression plasmid.

(E–G) qPCR, western blot, and the levels of ceramide analysis in HL60 and MOLM13 cells with control, BMAL1-OE or BMAL1-OE +IKZF2-OE. Cells were treated with or without RSL3 (0.5 μM) for 24 h. Data are presented as mean ± SD, $n = 3$ biologically independent samples.

Statistical tests used: (A and B), two-way ANOVA using Šídák multiple comparisons test with adjusted p values are shown. (C and D), one-way ANOVA using Dunnett multiple comparisons test with adjusted p values are shown. (E–G), two-way ANOVA using Tukey multiple comparisons test with adjusted p values are shown. $^*p < 0.05$, $^{**}p < 0.01$, $^{***}p < 0.001$, and $^{****}p < 0.0001$.

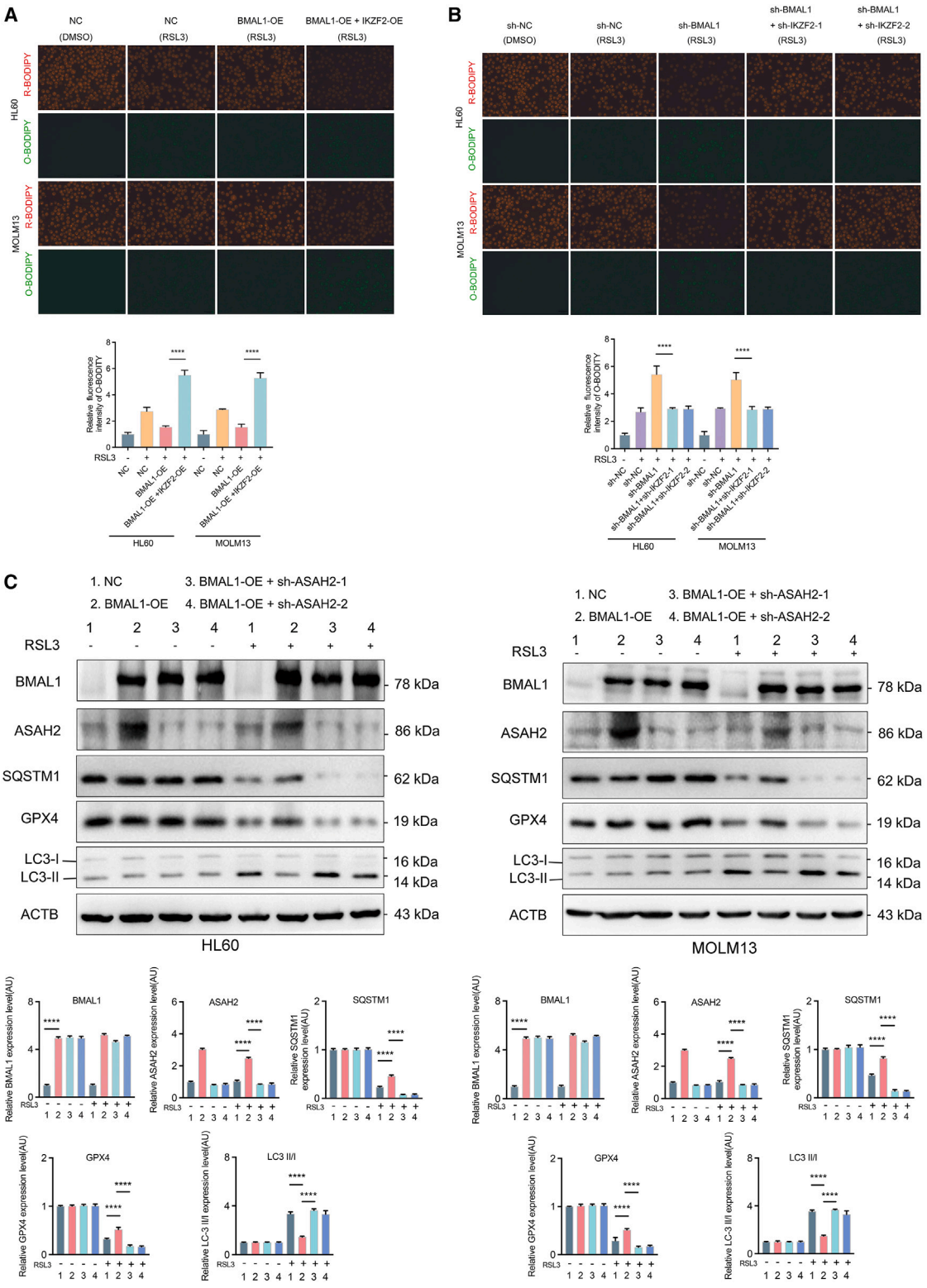

Figure 6. GPX4 degradation promotes ceramide upregulation-mediated ferroptosis

(A and B) The lipid ROS were assayed of HL60 and MOLM13 cells with vector, BMAL1-OE, BMAL1 shRNA, BMAL1-OE+IKZF2-OE, or BMAL1 +IKZF2 shRNA. Cells were treated with or without RSL3 (0.5 μM) for 24 h, Scale bar: 100 μm.

(legend continued on next page)

overexpression of IKZF2 or depletion of ASAH2 promoted ferroptosis and alleviated tumor burden (Figures 8B–8J and S12A–S12I). Contrarily, the depletion of IKZF2 suppresses ferroptosis, thereby exacerbating the tumor burden (Figures 8B–8J and S12A–S12I). The aforementioned findings were consistent with our *in vitro* results. Taken together, our AML animal model experiments provide compelling evidence that targeting BMAL1 can effectively induce tumor cell ferroptosis through the IKZF2-ASAH2 pathway, resulting in a potent anti-AML response. These findings hold significant promise for optimizing therapeutic strategies against AML targeting BMAL1.

DISCUSSION

BMAL1 serves as a suppressor of ferroptosis, and inhibiting it can promote ferroptosis. Furthermore, BMAL1 has been linked to tumor development and is considered an adverse prognostic factor for AML. AML cells are particularly sensitive to ferroptosis, making the targeting of BMAL1 an effective strategy for AML treatment. This study found that inhibiting BMAL1 can reshape ceramide metabolism through the IKZF2-ASAH2 pathway, ultimately promoting ferroptosis in AML cells and enhancing their sensitivity to the targeted drug sorafenib. These results highlight the potential of targeting BMAL1 as a promising approach in the development of anti-AML strategies.

GPX4 utilizes glutathione (GSH) as an essential cofactor to exert its antioxidant function, thus serving as a key determinant in protecting against ferroptosis.[43] Currently, the chemical compounds that trigger ferroptosis can be divided into two main categories: those that target the cystine/glutamate antiporter system (system Xc−) and those that target GPX4. The former class acts by impeding cystine uptake, leading to a reduction in GSH synthesis and subsequent GPX4 inactivation. When GPX4 function is impaired or lost, it can lead to the ineffective elimination of lipid peroxidation byproducts, resulting in their continuous accumulation, membrane damage, and eventual rupture. When investigating the promotion or inhibition of ferroptosis by a molecule, GPX4 is typically a primary focus. Targeting GPX4 to induce ferroptosis in tumor cells has proven to be an effective strategy for developing novel cancer therapies.[7,44,45] Ceramide has been shown to promote autophagy.[39] Thayyullathil et al. demonstrated that the elevation of ceramide levels, mediated by acid sphingomyelinase, enhances cellular autophagy and leads to GPX4 degradation, thereby promoting ferroptosis in tumor cells.[40] Furthermore, Ai-Hua Xu's team uncovered a correlation between osteoporosis in type 2 diabetes patients and ferroptosis in osteoblasts under high glucose conditions.[21] This mechanism involves high glucose inducing the activation of acid sphingomyelinase and an increase in ceramide levels, subsequently promoting cellular autophagy and GPX4 degradation, ultimately resulting in ferroptosis in osteoblasts. Therefore, based on these insights, we hypothesize that knocking down BMAL1 promotes AML cells ferroptosis, potentially through increased GPX4 degradation. Experiments validated our hypothesis. In this study, knocking down BMAL1 resulted in elevated ceramide levels during ferroptosis in AML cells, ultimately promoting the degradation of GPX4 and facilitating ferroptosis. This mechanism is consistent with the current majority of anticancer drugs that promote ferroptosis of tumor cells.

ASAH2 is the crucial enzyme involved in BMAL1-orchestrated regulation of ceramide metabolism. An increasing number of studies have found that ASAH2 is closely associated with tumors.[46] When ASAH2 activity is inhibited, ceramide levels increase, promoting the death of tumor cells.[47,48] Liangping Su et al. found that increased expression levels of β5 integrin are correlated with unfavorable prognosis and chemoresistance in both pancreatic and lung cancer.[49] Its resistance mechanism involves the upregulation of ASAH2 via β5 integrin, causing a decrease in ceramide levels and reduced ROS production, thereby inhibiting chemotherapy-induced pyroptosis. Administering a ceramidase inhibitor can restore tumor cell sensitivity to chemotherapy. Additionally, ASAH2 plays a role in enabling colon cancer MDSCs to evade ferroptosis by inhibiting the P53 pathway.[50] Zhongbin Deng's team discovered that in breast cancer, the decline of ASAH2 in myeloid cells triggers an upsurge in TREM2+ macrophages, where ceramide assumes a pivotal role.[51] This cascade ultimately fosters the emergence of enervated $CD8^+$ T cells, propelling tumor progression. Kumaran Sundaram et al. revealed that in mouse fibroblasts, depriving them of neutral ceramidase renders them resistant to necrotic cell death caused by nutrient deprivation.[52] This resistance mechanism involves increased ceramide levels, enhanced autophagy, and subsequent clearance of damaged proteins and organelles. Furthermore, Roberta Rosa's team uncovered that in colorectal cancer cells, elevated SPHK1-mediated reduction in ceramide levels leads to resistance to cetuximab.[53] Similar to prior research, our study demonstrated that upregulated ceramide facilitated the death of AML cells. Notably, in our research, we found that reducing BMAL1 led to the downregulation of ASAH2, resulting in elevated ceramide levels. This, in turn, enhanced autophagy and promoted the degradation of GPX4, subsequently facilitating ferroptosis in AML cells. Ultimately, ASAH2 mediates alterations in ceramide levels, thereby exerting regulatory influence over multiple downstream biological signaling cascades, ultimately determining the fate of tumor cell. The role of ASAH2 and ceramide varies across different tumor types, and further exploration is needed to understand their function in AML.

Ferroptosis has been observed in a range of cancer types, such as pancreatic cancer, colorectal cancer, and breast cancer.[54] Moreover, various therapeutic agents have shown the ability to induce ferroptosis. Sulfasalazine and sorafenib promote ferroptosis in hepatocellular carcinoma cells by inhibiting the function of SLC7A11.[55,56] Gemcitabine and cisplatin induce ferroptosis in pancreatic and colorectal cancer cells by selectively targeting GPX4.[57,58] Research findings have indicated

(C) Western blot analysis showing indicated protein expression in HL60 and MOLM13 cells with control, BMAL1-OE, or BMAL1-OE + ASAH2 shRNA. Cells were treated with or without RSL3 (0.5 μM) for 24 h. Data are presented as mean ± SD, $n = 3$ biologically independent samples.

Statistical tests used: (A and B), one-way ANOVA using Tukey multiple comparisons test with adjusted p values are shown. (C), two-way ANOVA using Tukey multiple comparisons test with adjusted p values is shown. *$p < 0.05$, **$p < 0.01$, ***$p < 0.001$, and ****$p < 0.0001$.

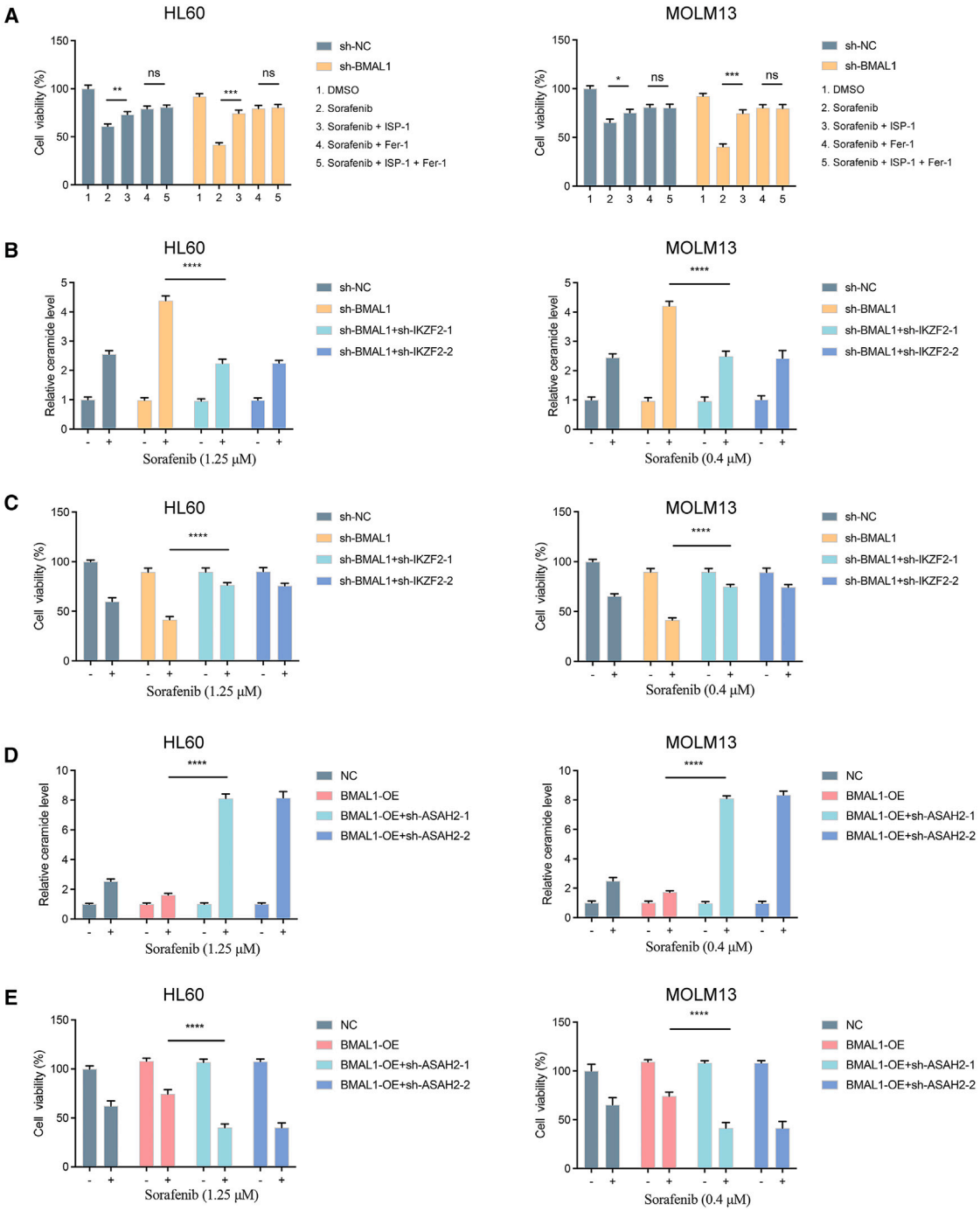

Figure 7. BMAL1 depletion boosts AML cell sensitivity to sorafenib

(A) Viability analysis of HL60 and MOLM13 cells with control or BMAL1 shRNA (versus blank control group). Cells were treated with sorafenib (1.25, 0.4 μM) in the presence or absence of myriocin (ISP-1, 1.0 μM) or ferrostain-1 (Fer-1, 0.5 μM) for 24 h. Before treating with sorafenib, the cells were pre-treated with ISP-1 for 24 h.

(B and C) The level of ceramide and viability analysis of HL60 and MOLM13 cells with control, BMAL1 shRNA or BMAL1+ IKZF2 shRNA (versus blank control group). Cells were treated with or without sorafenib (1.25, 0.4 μM) for 24 h.

(D and E) The level of ceramide and viability analysis of HL60 and MOLM13 cells with control, BMAL1-OE or BMAL1-OE+ASAH2 shRNA (versus blank control group). Cells were treated with or without sorafenib (1.25, 0.4 μM) for 24 h. Data are presented as mean ± SD, $n = 3$ biologically independent samples.

Statistical tests used: (A), two-way ANOVA using Šídák multiple comparisons test with adjusted p values is shown. (B–E), two-way ANOVA using Tukey multiple comparisons test with adjusted p values are shown. *$p < 0.05$, **$p < 0.01$, ***$p < 0.001$, and ****$p < 0.0001$.

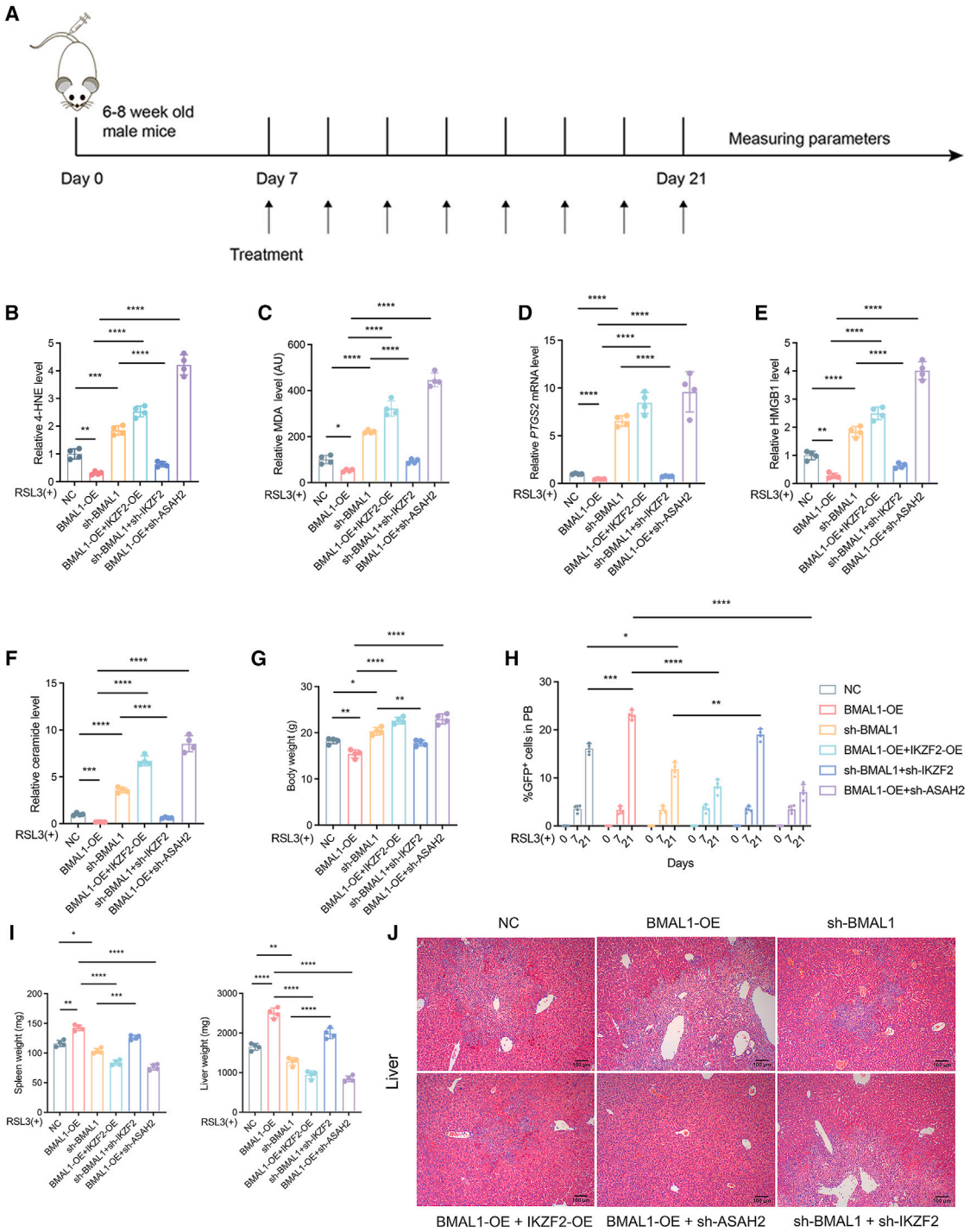

Figure 8. The BMAL1-IKZF2-ASAH2 pathway enhancing ferroptosis-mediated AML suppression in *vivo*

(A) The schematic diagram of the complete mouse experiment procedure.

(B–F) The level of 4-HNE (B), MDA (C), *PTGS2* mRNA (D), and ceramide (F) in the hepatic tumors tissue, and the level of serum HMGB1 (E) were assayed at the endpoint time after treatment (n = 4 mice/group).

(G) The weight of mice at the endpoint time after treatment (n = 4 mice/group).

(H) The GFP+ leukemia cells in peripheral blood of HL60 leukemia recipient mice at indicated days in treatment groups (n = 4 mice/group).

(legend continued on next page)

that etoposide's efficacy against AML stems from its induction of ferroptosis, achieved through the reduction of intracellular GSH levels and the inhibition of GPX4 activity.[59] Dihydroartemisinin enhances autophagy, leading to accelerated degradation of ferritin and promoting ferroptosis in AML cells.[60,61] Sulfasalazine, by targeting SLC7A11 and inhibiting cystine uptake, promotes cellular ferroptosis and enhances the efficacy of daunorubicin-cytarabine against AML.[62] Moreover, research has demonstrated that inhibition of SPHK results in an elevation of ceramide levels. The increased ceramide, by reducing MCL-1 expression through ATF4, facilitates tumor cell apoptosis, thereby enhancing the effectiveness of navitoclax and sorafenib against AML.[63] Overall, inducing tumor cells ferroptosis proves to be a highly effective strategy in the fight against cancer. Sorafenib, a ferroptosis-inducing agent and a frontline therapy for AML, frequently encounters drug resistance during treatment, posing a critical issue that demands immediate solution. In this study, the suppression of BMAL1 has been demonstrated to heighten intracellular ceramide levels, thereby promoting the sensitivity of AML cells to sorafenib. This discovery introduces a fresh perspective and trajectory for anti-AML research. Further investigations are warranted to explore the clinical implications of BMAL1 small molecule inhibitors.

Limitations of the study

This study utilized tumor cell lines to construct the tumor model, which differed to some extent from the actual tumor condition. It is worth exploring the potential use of a humanized immune system AML patient-derived xenograft (PDX) mouse model to investigate the function of BMAL1 and ceramide for AML drug resistance. Moreover, while short-chain C2-ceramide is a commonly employed surrogate in experiments for its ability to permeate cell membranes and modulate the intracellular ceramide pool,[64] it cannot fully replace the functions of natural ceramide. Hence, future studies could incorporate natural ceramide to more accurately validate the underlying mechanisms.

Conclusions

In essence, this research represents a significant advancement in identifying BMAL1, which modifies ceramide metabolism through the IKZF2-ASAH2 pathway, ultimately impacting ferroptosis in AML cells (Figure S13). Our study proposes a potential treatment approach for AML by combining BMAL1 inhibitors and ceramide. Further research is necessary to assess the clinical viability of BMAL1 inhibitors and ceramide, paving the way for their clinical implementation.

RESOURCE AVAILABILITY

Lead contact

Further information and requests for resources and reagents should be directed to and will be fulfilled or facilitated by the lead contact Minghua Yang (yangminghua@csu.edu.cn).

Materials availability

This study did not generate new unique reagents.

Data and code availability

- The accession code for lipidomic dataset is MetaboLights: MTBLS11557, and the corresponding URL is https://www.ebi.ac.uk/metabolights/MTBLS11557.
- This paper does not report original code.
- Any additional information required to reanalyze the data reported will be shared by the lead contact upon request.

ACKNOWLEDGMENTS

National Natural Science Foundation of China (81974000 and 82270185), the Science and Technology Innovation Program of Hunan Province (2022RC3077), Health Research Project of Hunan Provincial Health Commission (W20242008), and National Key Clinical Specialty Scientific Research Project (grant number: Z2023023) provided support for this study.

AUTHOR CONTRIBUTIONS

H.Z., conceptualization, methodology, investigation, resources, writing – original draft preparation, visualization, project administration; Z.L., methodology; D.W., methodology; J.Z., methodology; T.Z., methodology; J.S., methodology; J.-D.L., conceptualization, writing – reviewing and editing; supervision, project administration; M.Y., conceptualization, writing – reviewing and editing; supervision, project administration, funding acquisition. All authors contributed to this study. All authors reviewed the final version of the manuscript and agreed to its submission.

DECLARATION OF INTERESTS

All authors declare no competing interests.

STAR★METHODS

Detailed methods are provided in the online version of this paper and include the following:

- KEY RESOURCES TABLE
- EXPERIMENTAL MODEL AND STUDY PARTICIPANT DETAILS
  - Ethics approval and consent to participate
  - Human materials
  - Animals
- METHOD DETAILS
  - Cell culture
  - Human samples
  - Animal model
  - Untargeted lipidomic
  - Western blot
  - Real-time PCR
  - MDA
  - Lipid peroxidation
  - Chromatin immunoprecipitation
  - Cell viability assay
  - Lentivirus packaging and infection
  - Flow cytometry
  - Hematoxylin eosin staining
  - Bioinformatics analysis
- QUANTIFICATION AND STATISTICAL ANALYSIS

(I) The weight of liver and spleen in mice at the endpoint time after treatment (n = 4 mice/group).
(J) HE staining of liver of mice at the endpoint time after treatment. Scale bare: 100 μm. Data are presented as mean ± SD.
Statistical tests used: (B–G and I), one-way ANOVA using Tukey multiple comparisons test with adjusted p values are shown. (H), two-way ANOVA using Tukey multiple comparisons test with adjusted p values is shown. *$p < 0.05$, **$p < 0.01$, ***$p < 0.001$, and ****$p < 0.0001$.

SUPPLEMENTAL INFORMATION

Supplemental information can be found online at https://doi.org/10.1016/j.isci.2025.112054.

Received: August 11, 2024
Revised: November 17, 2024
Accepted: February 13, 2025
Published: March 22, 2025

REFERENCES

1. Newell, L.F., and Cook, R.J. (2021). Advances in acute myeloid leukemia. BMJ *375*, n2026. https://doi.org/10.1136/bmj.n2026.
2. DiNardo, C.D., Erba, H.P., Freeman, S.D., and Wei, A.H. (2023). Acute myeloid leukaemia. Lancet *401*, 2073–2086. https://doi.org/10.1016/s0140-6736(23)00108-3.
3. Jiang, X., Stockwell, B.R., and Conrad, M. (2021). Ferroptosis: mechanisms, biology and role in disease. Nat. Rev. Mol. Cell Biol. *22*, 266–282. https://doi.org/10.1038/s41580-020-00324-8.
4. Hadian, K., and Stockwell, B.R. (2023). The therapeutic potential of targeting regulated non-apoptotic cell death. Nat. Rev. Drug Discov. *22*, 723–742. https://doi.org/10.1038/s41573-023-00749-8.
5. Tang, D., Chen, X., Kang, R., and Kroemer, G. (2021). Ferroptosis: molecular mechanisms and health implications. Cell Res. *31*, 107–125. https://doi.org/10.1038/s41422-020-00441-1.
6. Liu, Y., Wan, Y., Jiang, Y., Zhang, L., and Cheng, W. (2023). GPX4: The hub of lipid oxidation, ferroptosis, disease and treatment. Biochim. Biophys. Acta Rev. Canc *1878*, 188890. https://doi.org/10.1016/j.bbcan.2023.188890.
7. Yang, W.S., SriRamaratnam, R., Welsch, M.E., Shimada, K., Skouta, R., Viswanathan, V.S., Cheah, J.H., Clemons, P.A., Shamji, A.F., Clish, C.B., et al. (2014). Regulation of ferroptotic cancer cell death by GPX4. Cell *156*, 317–331. https://doi.org/10.1016/j.cell.2013.12.010.
8. Chen, T.C., Chuang, J.Y., Ko, C.Y., Kao, T.J., Yang, P.Y., Yu, C.H., Liu, M.S., Hu, S.L., Tsai, Y.T., Chan, H., et al. (2020). AR ubiquitination induced by the curcumin analog suppresses growth of temozolomide-resistant glioblastoma through disrupting GPX4-Mediated redox homeostasis. Redox Biol. *30*, 101413. https://doi.org/10.1016/j.redox.2019.101413.
9. Sun, Y., Qiao, Y., Liu, Y., Zhou, J., Wang, X., Zheng, H., Xu, Z., Zhang, J., Zhou, Y., Qian, L., et al. (2021). ent-Kaurane diterpenoids induce apoptosis and ferroptosis through targeting redox resetting to overcome cisplatin resistance. Redox Biol. *43*, 101977. https://doi.org/10.1016/j.redox.2021.101977.
10. Chen, P., Li, X., Zhang, R., Liu, S., Xiang, Y., Zhang, M., Chen, X., Pan, T., Yan, L., Feng, J., et al. (2020). Combinative treatment of β-elemene and cetuximab is sensitive to KRAS mutant colorectal cancer cells by inducing ferroptosis and inhibiting epithelial-mesenchymal transformation. Theranostics *10*, 5107–5119. https://doi.org/10.7150/thno.44705.
11. Markowitsch, S.D., Schupp, P., Lauckner, J., Vakhrusheva, O., Slade, K.S., Mager, R., Efferth, T., Haferkamp, A., and Juengel, E. (2020). Artesunate Inhibits Growth of Sunitinib-Resistant Renal Cell Carcinoma Cells through Cell Cycle Arrest and Induction of Ferroptosis. Cancers *12*, 3150. https://doi.org/10.3390/cancers12113150.
12. Yang, M., Chen, P., Liu, J., Zhu, S., Kroemer, G., Klionsky, D.J., Lotze, M.T., Zeh, H.J., Kang, R., and Tang, D. (2019). Clockophagy is a novel selective autophagy process favoring ferroptosis. Sci. Adv. *5*, eaaw2238. https://doi.org/10.1126/sciadv.aaw2238.
13. Puram, R.V., Kowalczyk, M.S., de Boer, C.G., Schneider, R.K., Miller, P.G., McConkey, M., Tothova, Z., Tejero, H., Heckl, D., Järås, M., et al. (2016). Core Circadian Clock Genes Regulate Leukemia Stem Cells in AML. Cell *165*, 303–316. https://doi.org/10.1016/j.cell.2016.03.015.
14. Linder, S., Hoogstraat, M., Stelloo, S., Eickhoff, N., Schuurman, K., de Barros, H., Alkemade, M., Bekers, E.M., Severson, T.M., Sanders, J., et al. (2022). Drug-Induced Epigenomic Plasticity Reprograms Circadian Rhythm Regulation to Drive Prostate Cancer toward Androgen Independence. Cancer Discov. *12*, 2074–2097. https://doi.org/10.1158/2159-8290.Cd-21-0576.
15. Jiang, W., Jin, L., Ju, D., Lu, Z., Wang, C., Guo, X., Zhao, H., Shen, S., Cheng, Z., Shen, J., et al. (2022). The pancreatic clock is a key determinant of pancreatic fibrosis progression and exocrine dysfunction. Sci. Transl. Med. *14*, eabn3586. https://doi.org/10.1126/scitranslmed.abn3586.
16. Burgermeister, E., Battaglin, F., Eladly, F., Wu, W., Herweck, F., Schulte, N., Betge, J., Härtel, N., Kather, J.N., Weis, C.A., et al. (2019). Aryl hydrocarbon receptor nuclear translocator-like (ARNTL/BMAL1) is associated with bevacizumab resistance in colorectal cancer via regulation of vascular endothelial growth factor A. EBioMedicine *45*, 139–154. https://doi.org/10.1016/j.ebiom.2019.07.004.
17. Kuo, A., and Hla, T. (2024). Regulation of cellular and systemic sphingolipid homeostasis. Nat. Rev. Mol. Cell Biol. *25*, 802–821. https://doi.org/10.1038/s41580-024-00742-y.
18. Codini, M., Garcia-Gil, M., and Albi, E. (2021). Cholesterol and Sphingolipid Enriched Lipid Rafts as Therapeutic Targets in Cancer. Int. J. Mol. Sci. *22*, 726. https://doi.org/10.3390/ijms22020726.
19. Piazzesi, A., Afsar, S.Y., and van Echten-Deckert, G. (2021). Sphingolipid metabolism in the development and progression of cancer: one cancer's help is another's hindrance. Mol. Oncol. *15*, 3256–3279. https://doi.org/10.1002/1878-0261.13063.
20. Ogretmen, B. (2018). Sphingolipid metabolism in cancer signalling and therapy. Nat. Rev. Cancer *18*, 33–50. https://doi.org/10.1038/nrc.2017.96.
21. Du, Y.X., Zhao, Y.T., Sun, Y.X., and Xu, A.H. (2023). Acid sphingomyelinase mediates ferroptosis induced by high glucose via autophagic degradation of GPX4 in type 2 diabetic osteoporosis. Mol. Med. *29*, 125. https://doi.org/10.1186/s10020-023-00724-4.
22. Arora, S., Singh, P., Tabassum, G., Dohare, R., and Syed, M.A. (2022). miR-495-3p regulates sphingolipid metabolic reprogramming to induce Sphk1/ceramide mediated mitophagy and apoptosis in NSCLC. Free Radic. Biol. Med. *189*, 71–84. https://doi.org/10.1016/j.freeradbiomed.2022.07.001.
23. Blom, T., Li, S., Dichlberger, A., Bäck, N., Kim, Y.A., Loizides-Mangold, U., Riezman, H., Bittman, R., and Ikonen, E. (2015). LAPTM4B facilitates late endosomal ceramide export to control cell death pathways. Nat. Chem. Biol. *11*, 799–806. https://doi.org/10.1038/nchembio.1889.
24. Saddoughi, S.A., Gencer, S., Peterson, Y.K., Ward, K.E., Mukhopadhyay, A., Oaks, J., Bielawski, J., Szulc, Z.M., Thomas, R.J., Selvam, S.P., et al. (2013). Sphingosine analogue drug FTY720 targets I2PP2A/SET and mediates lung tumour suppression via activation of PP2A-RIPK1-dependent necroptosis. EMBO Mol. Med. *5*, 105–121. https://doi.org/10.1002/emmm.201201283.
25. Morad, S.A.F., Levin, J.C., Shanmugavelandy, S.S., Kester, M., Fabrias, G., Bedia, C., and Cabot, M.C. (2012). Ceramide–antiestrogen nanoliposomal combinations–novel impact of hormonal therapy in hormone-insensitive breast cancer. Mol. Cancer Therapeut. *11*, 2352–2361. https://doi.org/10.1158/1535-7163.Mct-12-0594.
26. Pyne, N.J., and Pyne, S. (2010). Sphingosine 1-phosphate and cancer. Nat. Rev. Cancer *10*, 489–503. https://doi.org/10.1038/nrc2875.
27. Lewis, A.C., Wallington-Beddoe, C.T., Powell, J.A., and Pitson, S.M. (2018). Targeting sphingolipid metabolism as an approach for combination therapies in haematological malignancies. Cell Death Dis. *4*, 72. https://doi.org/10.1038/s41420-018-0075-0.
28. Sundaramoorthy, P., Gasparetto, C., and Kang, Y. (2018). The combination of a sphingosine kinase 2 inhibitor (ABC294640) and a Bcl-2 inhibitor (ABT-199) displays synergistic anti-myeloma effects in myeloma cells without a t(11;14) translocation. Cancer Med. *7*, 3257–3268. https://doi.org/10.1002/cam4.1543.
29. Powell, J.A., Lewis, A.C., Zhu, W., Toubia, J., Pitman, M.R., Wallington-Beddoe, C.T., Moretti, P.A.B., Iarossi, D., Samaraweera, S.E., Cummings,

N., et al. (2017). Targeting sphingosine kinase 1 induces MCL1-dependent cell death in acute myeloid leukemia. Blood *129*, 771–782. https://doi.org/10.1182/blood-2016-06-720433.

30. Vijayan, Y., James, S., Viswanathan, A., Aparna, J.S., Bindu, A., Namitha, N.N., Anantharaman, D., Babu Lankadasari, M., and Harikumar, K.B. (2024). Targeting acid ceramidase enhances antitumor immune response in colorectal cancer. J. Adv. Res. *65*, 73–87. https://doi.org/10.1016/j.jare.2023.12.013.

31. Gencer, E.B., Ural, A.U., Avcu, F., and Baran, Y. (2011). A novel mechanism of dasatinib-induced apoptosis in chronic myeloid leukemia; ceramide synthase and ceramide clearance genes. Ann. Hematol. *90*, 1265–1275. https://doi.org/10.1007/s00277-011-1212-5.

32. Schwamb, J., Feldhaus, V., Baumann, M., Patz, M., Brodesser, S., Brinker, R., Claasen, J., Pallasch, C.P., Hallek, M., Wendtner, C.M., and Frenzel, L.P. (2012). B-cell receptor triggers drug sensitivity of primary CLL cells by controlling glucosylation of ceramides. Blood *120*, 3978–3985. https://doi.org/10.1182/blood-2012-05-431783.

33. Zheng, H., Wu, T., Lin, Z., Wang, D., Zhang, J., Zeng, T., Liu, L., Shen, J., Zhao, M., Li, J.D., and Yang, M. (2024). Targeting BMAL1 reverses drug resistance of acute myeloid leukemia cells and promotes ferroptosis through HMGB1-GPX4 signaling pathway. J. Cancer Res. Clin. Oncol. *150*, 231. https://doi.org/10.1007/s00432-024-05753-y.

34. Meng, Q., Hu, X., Zhao, X., Kong, X., Meng, Y.M., Chen, Y., Su, L., Jiang, X., Qiu, X., Huang, C., et al. (2021). A circular network of coregulated sphingolipids dictates lung cancer growth and progression. EBioMedicine *66*, 103301. https://doi.org/10.1016/j.ebiom.2021.103301.

35. Li, Y., Chaurasia, B., Rahman, M.M., Kaddai, V., Maschek, J.A., Berg, J.A., Wilkerson, J.L., Mahmassani, Z.S., Cox, J., Wei, P., et al. (2023). Ceramides Increase Fatty Acid Utilization in Intestinal Progenitors to Enhance Stemness and Increase Tumor Risk. Gastroenterology *165*, 1136–1150. https://doi.org/10.1053/j.gastro.2023.07.017.

36. Rasmussen, E.S., Takahashi, J.S., and Green, C.B. (2022). Time to target the circadian clock for drug discovery. Trends Biochem. Sci. *47*, 745–758. https://doi.org/10.1016/j.tibs.2022.04.009.

37. Stockwell, B.R. (2022). Ferroptosis turns 10: Emerging mechanisms, physiological functions, and therapeutic applications. Cell *185*, 2401–2421. https://doi.org/10.1016/j.cell.2022.06.003.

38. Liu, J., Tang, D., and Kang, R. (2024). Targeting GPX4 in ferroptosis and cancer: chemical strategies and challenges. Trends Pharmacol. Sci. *45*, 666–670. https://doi.org/10.1016/j.tips.2024.05.006.

39. Harvald, E.B., Olsen, A.S.B., and Færgeman, N.J. (2015). Autophagy in the light of sphingolipid metabolism. Apoptosis *20*, 658–670. https://doi.org/10.1007/s10495-015-1108-2.

40. Thayyullathil, F., Cheratta, A.R., Alakkal, A., Subburayan, K., Pallichankandy, S., Hannun, Y.A., and Galadari, S. (2021). Acid sphingomyelinase-dependent autophagic degradation of GPX4 is critical for the execution of ferroptosis. Cell Death Dis. *12*, 26. https://doi.org/10.1038/s41419-020-03297-w.

41. Chen, X., Kang, R., Kroemer, G., and Tang, D. (2021). Broadening horizons: the role of ferroptosis in cancer. Nat. Rev. Clin. Oncol. *18*, 280–296. https://doi.org/10.1038/s41571-020-00462-0.

42. Lu, B., Chen, X.B., Ying, M.D., He, Q.J., Cao, J., and Yang, B. (2017). The Role of Ferroptosis in Cancer Development and Treatment Response. Front. Pharmacol. *8*, 992. https://doi.org/10.3389/fphar.2017.00992.

43. Xie, Y., Kang, R., Klionsky, D.J., and Tang, D. (2023). GPX4 in cell death, autophagy, and disease. Autophagy *19*, 2621–2638. https://doi.org/10.1080/15548627.2023.2218764.

44. Li, K., Lin, C., Li, M., Xu, K., He, Y., Mao, Y., Lu, L., Geng, W., Li, X., Luo, Z., and Cai, K. (2022). Multienzyme-like Reactivity Cooperatively Impairs Glutathione Peroxidase 4 and Ferroptosis Suppressor Protein 1 Pathways in Triple-Negative Breast Cancer for Sensitized Ferroptosis Therapy. ACS Nano. *16*, 2381–2398. https://doi.org/10.1021/acsnano.1c08664.

45. Li, J., Liu, J., Zhou, Z., Wu, R., Chen, X., Yu, C., Stockwell, B., Kroemer, G., Kang, R., and Tang, D. (2023). Tumor-specific GPX4 degradation enhances ferroptosis-initiated antitumor immune response in mouse models of pancreatic cancer. Sci. Transl. Med. *15*, eadg3049. https://doi.org/10.1126/scitranslmed.adg3049.

46. Gu, X., Sun, R., Chen, L., Chu, S., Doll, M.A., Li, X., Feng, W., Siskind, L., McClain, C.J., and Deng, Z. (2021). Neutral Ceramidase Mediates Nonalcoholic Steatohepatitis by Regulating Monounsaturated Fatty Acids and Gut IgA(+) B Cells. Hepatology *73*, 901–919. https://doi.org/10.1002/hep.31628.

47. Coant, N., García-Barros, M., Zhang, Q., Obeid, L.M., and Hannun, Y.A. (2018). AKT as a key target for growth promoting functions of neutral ceramidase in colon cancer cells. Oncogene *37*, 3852–3863. https://doi.org/10.1038/s41388-018-0236-x.

48. García-Barros, M., Coant, N., Kawamori, T., Wada, M., Snider, A.J., Truman, J.P., Wu, B.X., Furuya, H., Clarke, C.J., Bialkowska, A.B., et al. (2016). Role of neutral ceramidase in colon cancer. FASEB J. *30*, 4159–4171. https://doi.org/10.1096/fj.201600611R.

49. Su, L., Chen, Y., Huang, C., Wu, S., Wang, X., Zhao, X., Xu, Q., Sun, R., Kong, X., Jiang, X., et al. (2023). Targeting Src reactivates pyroptosis to reverse chemoresistance in lung and pancreatic cancer models. Sci. Transl. Med. *15*, eabl7895. https://doi.org/10.1126/scitranslmed.abl7895.

50. Zhu, H., Klement, J.D., Lu, C., Redd, P.S., Yang, D., Smith, A.D., Poschel, D.B., Zou, J., Liu, D., Wang, P.G., et al. (2021). Asah2 Represses the p53-Hmox1 Axis to Protect Myeloid-Derived Suppressor Cells from Ferroptosis. J. Immunol. *206*, 1395–1404. https://doi.org/10.4049/jimmunol.2000500.

51. Sun, R., Lei, C., Xu, Z., Gu, X., Huang, L., Chen, L., Tan, Y., Peng, M., Yaddanapudi, K., Siskind, L., et al. (2024). Neutral ceramidase regulates breast cancer progression by metabolic programming of TREM2-associated macrophages. Nat. Commun. *15*, 966. https://doi.org/10.1038/s41467-024-45084-7.

52. Sundaram, K., Mather, A.R., Marimuthu, S., Shah, P.P., Snider, A.J., Obeid, L.M., Hannun, Y.A., Beverly, L.J., and Siskind, L.J. (2016). Loss of neutral ceramidase protects cells from nutrient- and energy -deprivation-induced cell death. Biochem. J. *473*, 743–755. https://doi.org/10.1042/bj20150586.

53. Rosa, R., Marciano, R., Malapelle, U., Formisano, L., Nappi, L., D'Amato, C., D'Amato, V., Damiano, V., Marfè, G., Del Vecchio, S., et al. (2013). Sphingosine kinase 1 overexpression contributes to cetuximab resistance in human colorectal cancer models. Clin. Cancer Res. *19*, 138–147. https://doi.org/10.1158/1078-0432.Ccr-12-1050.

54. Lei, G., Zhuang, L., and Gan, B. (2022). Targeting ferroptosis as a vulnerability in cancer. Nat. Rev. Cancer *22*, 381–396. https://doi.org/10.1038/s41568-022-00459-0.

55. Sun, X., Ou, Z., Chen, R., Niu, X., Chen, D., Kang, R., and Tang, D. (2016). Activation of the p62-Keap1-NRF2 pathway protects against ferroptosis in hepatocellular carcinoma cells. Hepatology *63*, 173–184. https://doi.org/10.1002/hep.28251.

56. Sun, X., Niu, X., Chen, R., He, W., Chen, D., Kang, R., and Tang, D. (2016). Metallothionein-1G facilitates sorafenib resistance through inhibition of ferroptosis. Hepatology *64*, 488–500. https://doi.org/10.1002/hep.28574.

57. Zhu, S., Zhang, Q., Sun, X., Zeh, H.J., 3rd, Lotze, M.T., Kang, R., and Tang, D. (2017). HSPA5 Regulates Ferroptotic Cell Death in Cancer Cells. Cancer Res. *77*, 2064–2077. https://doi.org/10.1158/0008-5472.Can-16-1979.

58. Guo, J., Xu, B., Han, Q., Zhou, H., Xia, Y., Gong, C., Dai, X., Li, Z., and Wu, G. (2018). Ferroptosis: A Novel Anti-tumor Action for Cisplatin. Cancer Res. Treat. *50*, 445–460. https://doi.org/10.4143/crt.2016.572.

59. Kagan, V.E., Mao, G., Qu, F., Angeli, J.P.F., Doll, S., Croix, C.S., Dar, H.H., Liu, B., Tyurin, V.A., Ritov, V.B., et al. (2017). Oxidized arachidonic and adrenic PEs navigate cells to ferroptosis. Nat. Chem. Biol. *13*, 81–90. https://doi.org/10.1038/nchembio.2238.

60. Du, J., Wang, T., Li, Y., Zhou, Y., Wang, X., Yu, X., Ren, X., An, Y., Wu, Y., Sun, W., et al. (2019). DHA inhibits proliferation and induces ferroptosis of leukemia cells through autophagy dependent degradation of ferritin. Free Radic. Biol. Med. *131*, 356–369. https://doi.org/10.1016/j.freeradbiomed.2018.12.011.

61. Grignano, E., Cantero-Aguilar, L., Tuerdi, Z., Chabane, T., Vazquez, R., Johnson, N., Zerbit, J., Decroocq, J., Birsen, R., Fontenay, M., et al. (2023). Dihydroartemisinin-induced ferroptosis in acute myeloid leukemia: links to iron metabolism and metallothionein. Cell Death Dis. *9*, 97. https://doi.org/10.1038/s41420-023-01371-8.

62. Pardieu, B., Pasanisi, J., Ling, F., Dal Bello, R., Penneroux, J., Su, A., Joudinaud, R., Chat, L., Wu, H.C., Duchmann, M., et al. (2022). Cystine uptake inhibition potentiates front-line therapies in acute myeloid leukemia. Leukemia *36*, 1585–1595. https://doi.org/10.1038/s41375-022-01573-6.

63. Lewis, A.C., Pope, V.S., Tea, M.N., Li, M., Nwosu, G.O., Nguyen, T.M., Wallington-Beddoe, C.T., Moretti, P.A.B., Anderson, D., Creek, D.J., et al. (2022). Ceramide-induced integrated stress response overcomes Bcl-2 inhibitor resistance in acute myeloid leukemia. Blood *139*, 3737–3751. https://doi.org/10.1182/blood.2021013277.

64. Summers, S.A., Chaurasia, B., and Holland, W.L. (2019). Metabolic Messengers: ceramides. Nat. Metab. *1*, 1051–1058. https://doi.org/10.1038/s42255-019-0134-8.

65. Bhasin, J. (2006). The CCAC Guidelines on Choosing an Appropriate Endpoint in Experiments Using Animals for Research, Teaching, and Testing. Developed by the Ad Hoc Subcommittee on Endpoints of the CCAC Guidelines. http://www.ccac.ca/en/CCAC_Programs/Guidelines_Policies/PDFs/APPOPEN.pdf.

66. Workman, P., Aboagye, E.O., Balkwill, F., Balmain, A., Bruder, G., Chaplin, D.J., Double, J.A., Everitt, J., Farningham, D.A.H., Glennie, M.J., et al. (2010). Guidelines for the welfare and use of animals in cancer research. Br. J. Cancer. *102*, 1555–1577. https://doi.org/10.1038/sj.bjc.6605642.

67. (1989). UKCCCR Guidelines for the Welfare of Animals in Experimental Neoplasia. ILAR J. *31*, 16–23. https://doi.org/10.1093/ilar.31.3.16.

68. Mizuno, H., Kitada, K., Nakai, K., and Sarai, A. (2009). PrognoScan: a new database for meta-analysis of the prognostic value of genes. BMC Med. Genom. *2*, 18. https://doi.org/10.1186/1755-8794-2-18.

STAR★METHODS

KEY RESOURCES TABLE

REAGENT or RESOURCE	SOURCE	IDENTIFIER
Antibodies		
BMAL1	Cell signaling technology	RRID:AB_2728705
IKZF2	Cell signaling technology	RRID:AB_2799221
SQSTM1	Cell signaling technology	RRID:AB_2799160
LCA/B	Cell signaling technology	RRID:AB_2617131
Anti-rabbit IgG	Cell signaling technology	RRID:AB_2099233
GPX4	Abcam	RRID:AB_10973901
ASAH2	Abcam	RRID:AB_2058852
β-actin	Abcam	RRID:AB_2223210
Biological samples		
Human PBMC and BM samples	the Third Xiangya Hospital, Central South University	This paper
Chemical, peptides, and recombinants proteins		
BCA Protein Assay Kits	Thermo Fisher Scientific	Cat#23225
RIPA lysis buffer	Beyotime	Cat#P0013B
PVDF membrances	Millipore	Cat#IPFL00010
Fetal bovine serum	Gibco™	Cat#A5670701
RPMI 1640	Gibco™	Cat#11875119
Penicillin-streptomycin	Beyotime	Cat#C0222
Lipo8000™ Transfection Reagent	Beyotime	Cat# C0533-1.5ml
RSL3	Selleck	Cat#S8155
Sorafenib	Selleck	Cat#S7397
Hydroxychloroquine	Selleck	Cat#S4430
Ferrostain-1	Selleck	Cat#S7243
C2 Ceramide	MCE	Cat#HY-101180
Myriocin	MCE	Cat#HY-N6798
MDA	Beyotime	Cat# S0131M
BSA	Thermo Fisher Scientific	Cat#11021029
Hematoxylin stain	Beyotime	Cat#C0107-100ml
Eosin stain	Beyotime	Cat#C0109
4% paraformaldehyde	Servicebio	Cat#G1101-500ML
Lipid Peroxidation Probe -BDP 581/591 C11	Dojindo	Cat#L267
30% Gelatin Buffer Solution 29:1	Beijing Dingguo Changsheng Biotechnology Co., Ltd.	Cat#MMR007
1.0M Tris-HCl pH6.8	Beijing Dingguo Changsheng Biotechnology Co., Ltd.	Cat# WB-0021
1.5M Tris-HCl pH8.8	Beijing Dingguo Changsheng Biotechnology Co., Ltd.	Cat# WB-0013
TEMED	Sangon Biotech	Cat#A610508-0025
Isopropyl Alcohol	Chron chemicals	Cat# 67-63-0
Ethyl Alcohol	Chron chemicals	Cat#64-17-5
Trichloromethane	Chron chemicals	Cat#67-66-3
Methyl alcohol	Chron chemicals	Cat# 67-56-1
Tween 20	Yeasen Biotechnology (Shanghai)	Cat#60305ES76

(*Continued on next page*)

Continued

REAGENT or RESOURCE	SOURCE	IDENTIFIER
lumiBest Superior ECL Luminescence Reagent	Share-bio	Cat#SB-WB011
Puromycin	Thermo Fisher Scientific	Cat#A1113803
Polybrene	Beyotime	Cat#C0351-1ml
TRIzol	Thermo Fisher Scientific	Cat#15596026CN
PrimeScript™ RT reagent Kit (Perfect Real Time)	Takara	Cat#RR037A
Hieff® qPCR SYBR Green Master Mix (No Rox)	Yeasen Biotechnology (Shanghai)	Cat#11201ES08
Critical commerical assay		
Cell Counting kit-8	Abiowell	Cat#AWC0114
Firefly & Renilla Luciferase Reporter Assay Kit	Meilunbio	Cat#MA0518-2
4-HNE ELISA Kit	Jonlnbio	Cat# JL46304
Ceramide ELISA Kit	mlbio	Cat#ml037872
Human HMGB-1(High Mobility group protein B1) ELISA Kit	Elabscience	Cat#E-EL-H1554
ChIP assay kit	Abcam	Cat#ab500
Experimental models: Cell lines		
HL60	The Cell Resource Center, Peking Union Medical College	RRID: CVCL_0002
MOLM13	The Cell Resource Center, Peking Union Medical College	RRID: CVCL_2119
Experimental models: Organisms/strains		
BALB/c nude mice	Changsha Slac Jingda Laboratory Animal Co., Ltd.	N/A
Oligonucleotides		
Primers used for real-time PCR,list in Table S3	this paper	N/A
Software and algorithms		
GraphPad Prism 9.0	GraphPad	N/A
FACSVerse flow cytometry system	BD Biosciences	N/A
ImageJ software	ImageJ	N/A
CFX Manager™	BIO-RAD	N/A
Other		
lipidomic dataset	This paper	https://www.ebi.ac.uk/metabolights/MTBLS11557.

EXPERIMENTAL MODEL AND STUDY PARTICIPANT DETAILS

Ethics approval and consent to participate

The human samples involved in this study were approved by the Ethics Committee of the Third Xiangya Hospital of Central South University (Q.24058). All participants provided written informed consent.

Human materials

The bone marrow for all research designs was sourced from AML patients, and the peripheral blood was obtained from healthy volunteers. The study received approval from the Ethics Committee of the Third Xiangya Hospital, Central South University. All participants provided signed informed consent. The clinical information of the participants can be found in Table S2.

Animals

The animal experiments were approved by the Animal Experiment Ethics Committee of the Third Xiangya Hospital of Central South University (IACUC.2021-159), ensuring compliance with ethical guidelines. The mice were kept in a pathogen-free barrier facility with

daily cleaning and weekly pathogen testing. They were exposed to a 12-hour light-dark cycle and had access to plentiful food and water. Each cage housed five mice, and all procedures involving the mice during the experiment adhered to principles of animal welfare. Male nude mice, ranging in age from 6 to 8 weeks, were sourced from Hunan SJA Laboratory Animal Co., Ltd. for utilization in the experiment.

METHOD DETAILS

Cell culture

Acute myeloid leukemia cells HL60(RRID: CVCL_0002), MOLM13(RRID: CVCL_2119) were acquired from the Cell Resource Center, Peking Union Medical College (PCRC). HL60, MOLM13 were cultured using RPMI1640 medium,1% Penicillin-Streptomycin antibiotic. The cell lines were all verified by STR typing every year and tested negative for mycoplasma. The cells were incubated in a sterile and humidified incubator at 37°C with 5% CO2. To facilitate cell spreading, 6-well plates were utilized, with each well containing 5✖ 105 cells and a volume of 2 ml. The cell culture plates were placed in a specialized incubator for cell cultivation. Following that, the cells were gathered by means of centrifugation after the appropriate time of action, or continued for other purposes. All experimental operations were carried out on an ultra-clean bench and all experimental equipment was sterilized. The experimental personnel were strictly adhering to the aseptic operation norms.

Human samples

This study was approved by the Ethics Committee of the Third Xiangya Hospital of Central South University (Q.24058). Written consent was obtained from each donor of human tissue samples used in this study, and all methods adhered to the Declaration of Helsinki. The healthy control group consisted of 6 samples, while each of the other groups included 9 samples. Participants were randomly assigned to the experimental and control groups using a simple randomization method. The samples for the healthy control group were peripheral blood. The samples for newly diagnosed, remitted, and relapsed patients were bone marrow. Specifically, the bone marrow samples from newly diagnosed patients were selected to have a $CD34^+$ proportion greater than 90%. To isolate mononuclear cells from peripheral blood or bone marrow, label a 15 mL centrifuge tube and add 4 mL of lymphocyte separation medium per tube. Take 4 mL of fresh bone marrow/blood, dilute with PBS at a 1:1 ratio, and mix well. Slowly add the diluted anticoagulated blood to the upper layer of the lymphocyte separation medium along the tube wall, then centrifuge at 500g for 25-30 minutes at room temperature. After centrifugation, three layers will form: the top layer contains plasma and PBS, the bottom layer contains red blood cells and granulocytes, and the middle layer contains the lymphocyte separation medium. A white cloudy layer of mononuclear cells (mainly lymphocytes and monocytes, with some platelets) will be visible at the interface of the top and middle layers. Remove some of the top layer liquid, leaving approximately 1 mL, and use a pipette to collect the mononuclear cell layer. Transfer to a new 15 mL centrifuge tube, add 10 mL PBS, mix well, and centrifuge at 500g for 5 minutes. Discard the supernatant. If there are many red blood cells, add 3-5 times the cell volume of red blood cell lysis buffer, incubate at room temperature for 5 minutes, and centrifuge at 500g for 5 minutes. Discard the supernatant. Finally, resuspend the cells in 1 mL PBS, mix well, centrifuge at 500g for 5 minutes, and discard the supernatant.

Animal model

GFP-labeled HL60 cells were administered to the mice via tail vein injection at a concentration of 2×10^6 cells per mouse. After a seven-day period, the mice were assessed and randomly assigned to different groups (simple randomization). Throughout the entire experiment and the data analysis process, the experimenters were blinded to the group assignments. ① The mice assessing the impact of BMAL1 on survival received no additional therapeutic interventions. Daily monitoring and recording of their survival status was conducted, with euthanasia performed when the score met the criteria for an endpoint, as specified by animal welfare guidelines in tumor research.[65–67] ② The mice underwent RSL3 drug therapy, administered through intraperitoneal injections at a dosage of 30 mg/kg every two days for a duration of two weeks. The drug formulation process followed the recommended guidelines provided by the manufacturer. And the untreated group received corresponding solvent injections. After the completion of the drug treatment, specific tissues from the mice were collected for the assessment of various indicators. Peripheral blood was collected via the enucleation method. Mice were euthanized by cervical dislocation, and their liver tumor tissue was quickly excised under sterile conditions on ice. Blood samples were processed and analyzed according to the protocol provided by the HMGB1 ELISA kit. Liver tumor tissues were processed and analyzed using the established protocols for the 4-HNE, MDA, and ceramide assay kits. Detailed information on these kits can be found in the ‘‘key resources table’’ section. The specific procedure for hematoxylin and eosin (H&E) staining of liver tumor tissue is described in the "hematoxylin eosin staining" section. Total RNA from liver tumor tissues was extracted using the TRIzol method. The procedure was as follows: an appropriate amount of tumor tissue was excised and placed into a 1.5 mL centrifuge tube, which was then labeled with the mouse group, sample number, experiment date, and experimenter’s name. The tube was subsequently snap-frozen in liquid nitrogen. All subsequent procedures were performed in a dedicated RNA extraction workstation. The 1.5 mL centrifuge tube was placed on an ice box, and 100 μL of TRIzol was added. The tissue was homogenized thoroughly using a handheld tissue grinder. An additional 900 μL of TRIzol was used to wash the grinder rod, ensuring full recovery of any remaining tissue. A new grinder rod was used for each sample to prevent

cross-contamination. After mixing thoroughly, the sample was left on ice for 10 minutes. For every 1000 μL of TRIzol, 200 μL of chloroform was added, and the mixture was shaken vigorously. Subsequent steps are described in the "real-time PCR" section.

Untargeted lipidomic

Initially, we successfully acquired HL60 cells with efficient knockdown of BMAL1 through the shRNA lentivirus, as outlined in the "lentivirus packaging and infection" section. Subsequently, we plated both control and BMAL1-knockdown HL60 cells in optimal growth condition onto 10-cm dishes at a density of 1×10^7 cells per dish. To guarantee a sufficient cell count for sequencing (>1×10^7 cells per sample), we grouped two dishes of cells as one set. These cells were then treated with RSL3 (0.5 μM) for a duration of 24 hours. Following the completion of drug treatment, the cells from the two dishes within each set were collected into a 1.5 ml centrifuge tube at 2000 rpm for 3 minutes. The cells were then washed three times with 1 ml of DPBS per tube. After thoroughly removing the DPBS, the cells were promptly frozen in liquid nitrogen and stored at -80°C. The samples were prepared for sequencing one day after being stored. Combine the cell sample with 200 μL of chilled water, 20 μL of lipid internal standard mixture, and 800 μL of cold methyl tert-butyl ether. Gently agitate the mixture for 30 seconds using a vortexer. Subsequently, introduce 240 μL of methanol and continue vortexing for an additional 30 seconds. Subject the sample to ultrasonication at a temperature of 4°C for a duration of 20 minutes, and subsequently, incubate it for 30 minutes. To extract lipids, centrifuge the sample at 10°C for 15 minutes at a speed of 14,000 g. Following centrifugation, use a vacuum centrifuge to dry the upper organic layer. Prior to analysis, reconstitute the lipid extract in a solution containing isopropanol and acetonitrile, with a volume ratio of 9:1. To perform untargeted lipidomic, the extracted sample was subjected to liquid chromatography-mass spectrometry. Specifically, the lipids were separated using a Waters ACQUITY PREMIER CSH C18 column (1.7 μm, 2.1*100 mm) under specific chromatographic conditions. The mobile phase used for separation comprised of a mixture of acetonitrile and water (in a 6:4 volume ratio as phase A) and a mobile phase of acetonitrile and isopropanol (in a 1:9 volume ratio as phase B). The mobile phase was applied at a flow rate of 300 μL/min, while the column temperature was maintained at 45°C throughout the analysis. The gradient elution process was initiated with a composition of 30% B and held for 2 minutes. Subsequently, a linear increase to 100% B was achieved over a period of 23 minutes. The gradient was then returned to 30% B within 1 minute, followed by a 9-minute equilibration period. The samples were kept in an autosampler at a constant temperature of 10°C throughout the analysis. To minimize signal fluctuations, a random injection sequence was employed. Mass spectrometric detection was conducted using a Thermo ScientificTM Q Exactive mass spectrometer featuring an electrospray ionization (ESI) source. Data acquisition was performed in both positive and negative ionization modes. To analyze the lipidome, we implemented a data-dependent acquisition (DDA) approach for MS/MS analysis. After each full MS1 scan, we recorded 10 MS2 scans. The resolution was set at 70,000 at m/z 200 for MS1 and 17,500 at m/z 200 for MS2. Additionally, we utilized ESI settings that included a heater. The LipidSearch platform was utilized to perform peak identification, peak extraction, and lipid identification for both lipid molecules and internal standard lipid molecules. Before analysis, a thorough quality assessment was conducted on the data. R 4.3.0 was then utilized for data analysis and image acquisition.

Western blot

Following cell collection, a double wash was performed using pre-cooled PBS. The required volume of RIPA lysate was then added, and the cell lysate was subjected to sonication. The cells were subsequently lysed for 30 minutes at a temperature of 4°C. The supernatant was collected (Conditions:10 minutes, 4°C, 12,000 rpm.). Protein quantification was performed using BCA method. The 8%-12% concentration of SDS-PAGE gel for western blot. 30-40 μg protein per well. The electrophoresis conditions: 80 volts for 30 minutes, followed by 120 volts for 90 minutes. Wet transfer was used to transfer protein. The transfer membrane conditions: 290 milliamps for 90 minutes. PVDF membrane was used. The blocking buffer is 5% skim milk with 0.1% concentration of TBAT. The environment was 4°C for 2 hours. After the blocking step, the target antibody was used for incubation at 4°C overnight. The secondary antibody used the 5% skim milk with a dilution ratio of 1: 5 000. Incubation conditions of secondary antibody was 4°C for 2 hours. After using 0.1%TBST to wash the membrane for 3 times, wash with TBS for the last time. Pierce stripes are visualized using the ECL Western Blotting Substrate kit. ImageJ software was used for quantitative analysis. The control protein using Actin.

Real-time PCR

After corresponding treatment, HL60, MOLM13 cells were collected by centrifugation. Total RNA of cells was extracted by TRIZOL method. Each sample was added with 1000 μL of TRIzol and incubated on ice for 5 minutes. Then, 200μL of chloroform was added, followed by vigorous shaking for 15 seconds and incubation on ice for 3 minutes. Centrifugation was performed at 4°C for 15 minutes at 12,000g. The upper aqueous phase was transferred to a new EP tube and mixed with an equal volume of isopropanol, then placed at -20°C for 30 minutes. Subsequent centrifugation was conducted at 4°C for 10 minutes at 13,000g, and the supernatant was discarded. The precipitate was gently washed twice with 1mL of 75% ethanol (prepared with DEPC water) under centrifugation at 7,000g for 5 minutes each time. Finally, the supernatant was discarded, and after complete ethanol evaporation, 7μL of DEPC water was added to dissolve the RNA. Takara kit was used for reverse transcription. After reverse transcription, SYBR Green Master Mix kit was used for qPCR. Gene expression analysis was standardized by the control gene *ACTB*.

MDA

We employed the Beyotime MDA (malondialdehyde) lipid oxidation kit for our study. The experimental procedures adhered to the manufacturer's protocol. Tissue or cell samples were lysed using a western blot lysate solution. For tissue, the weight of tissue accounts for 10% of the lysate. For cells, 0.1ml lysate was used for every one million cells. The supernatant was collected by centrifuging the samples at 12,000g for 10 minutes at 4°C. Following sample preparation, the protein concentration was determined. The sample was subjected to a heat treatment at 100°C for 15 minutes using a water bath. Afterward, the sample was allowed to cool down to room temperature in the same water bath, and the supernatant was collected by centrifugation at 1000g for 10 minutes. Add 200 μL supernatant to the 96-well plate. The absorbance was determined by a Microplate Reader at 532nm.

Lipid peroxidation

Lipid Peroxidation Probe-BDP 581 Universe 591 C11 kit (Dojindo, L267) was employed as a tool to carry out the experiment. For experimental operation, refer to the manufacturer protocol. After cell counting using a cytometer, HL60 and MOLM13 cells with vigorous growth were seeded at a concentration of 2×10^5 cells/ml in 8-well plates. Subsequently, the appropriate drugs were introduced for treatment. The cell culture plates were kept in a temperature-controlled incubator set at 37°C with a 5% CO2 atmosphere for the specified period. The supernatant was removed after centrifugation to collect cells (1000r, 3 mins). Wash the cells with 1640 medium 1 ml for 2 times. BDP 581x591 C11 working buffer was used to re-suspend cells. Put the plate back to the incubator for 30 mins. Following that, the supernatant was eliminated through centrifugation, and the cells were subjected to two washes using phenol red-free HBSS 1 ml. Cells were re-suspended by adding HBSS 1 ml, and subsequently, a fluorescence microscope was employed for observation and image capture within 30 minutes.

Chromatin immunoprecipitation

We used ChIP kit to carry out the experiment. The experimental procedure followed the protocol of the manufacturer. The first step was cell fixation and collection. For cell fixation, the cell culture dish was supplemented with an equivalent volume of 37% formaldehyde, resulting in a final concentration of 1%. At the end of fixation, add glycine to neutralize unreacted formaldehyde. Following a pre-cooled PBS wash and subsequent centrifugation, the cells were gathered. Subsequently, appropriate treatments were applied before proceeding with sonication. Cut the DNA into fragments of 200 - 1000 bp in size using an ultrasonic breaker. Make sure to keep the sample at 4°C throughout the sonication process. Third, the corresponding antibodies were added to the chromatin for cross-linking at 4°C overnight. Fourth, the antibody-chromatin was cross-linked with the magnetic beads at 4°C for 4h. At the end of cross-linking, DNA was purified using magnetic beads. The DNA samples obtained from purification were subjected to real time quantitative.

Cell viability assay

HL60 and MOLM13 cells, characterized by favorable growth status, were harvested via centrifugation and subsequently resuspended using PBS. The cell density was quantified using a cell counting plate. Upon application of the specific conditions, the cells were transferred to 96-well plates at a density of 5*104 cells per well for seeding. The plates were subjected to incubation for the specified duration in an incubator maintained at 37°C with 5% CO2. Upon completion of the specified duration, 10 μL of CCK8 detection reagent was meticulously added to each well and gently mixed. The 96-well plates were then repositioned in the incubator for an additional 1.5-2 hours. Ultimately, the absorbance at 450 nm was assessed using a Microplate Reader.

Lentivirus packaging and infection

We used well-grown 293T cells for lentiviral packaging. At the outset, 293T cells were introduced into a 10cm dish on the initial day. The suitable seeding density was 70-80% of the cells growing to 10 cm dishes after 24 hours. The day after, a specific ratio of the packaging plasmid and the target plasmid was delivered into 293T cells through transfection (pVSV-G: psPAX2: target plasmid =1:3:2,totaling 15 μg/ dish). The transfection reagent was lipo8000. The virus was collected 48 hours after transfection. Viral processing conditions: 400g, 4min.Then filter it through a 0.45μm filter. If used immediately, it can be stored for up to a week at 4°C. If long-term storage is required, dispense and store in a -80°C refrigerator. When the virus was used to infect cells, the ratio of virus to medium was 1:1. The concentration of polybrene was 10μg/ml. The cells were infected for 24 hours and then replaced with a new virus and infected for another 24 hours. At the end of the infection, puromycin was added for screening for 3 days. Finally, infection efficiency was determined using qPCR or western blot.

Flow cytometry

A suitable number of cells were seeded in a 6-well plate and subjected to the corresponding conditions for the necessary time period. Afterward, the cells were harvested by centrifugation and and subjected to two rounds of washing with pre-cooled PBS. Each tube was supplemented with 100 μL of 1× binding buffer, and the cells were then resuspended using a pipette gun. The dye should be added while avoiding exposure to light. The non-stained group does not receive any dye, the single-stained group is treated with either Annexin V or PI, and the double-stained group is treated with both Annexin V and PI. The mixture should be gently mixed using a pipette gun.Upon completion of a 15-minute incubation period at room temperature, ensuring adequate protection from any light exposure, an additional 300 μL of 1× binding buffer was introduced. After a thorough blending process, the cell suspension was

meticulously relocated to 5 mL flow tubes, ensuring complete shielding from any light interference. Subsequently, within a time frame of one hour, the samples were expeditiously subjected to analysis using a state-of-the-art flow cytometer. The gating strategy for apoptosis detection involved the use of two single-stained tubes to separate negative cells, ensuring that over 95% of the cells were distributed in the LL quadrant. Annexin V single staining ensured that over 95% of the cells were distributed in the LL+LR quadrants, while PI single staining ensured that over 95% of the cells were distributed in the LL+UL quadrants.

Hematoxylin eosin staining

After the mice tissues were extracted, they were fixed in paraformaldehyde for more than 24h, and gradient dehydration was performed after the fixation was completed. After dehydration, the tissue was embedded in paraffin and sliced. The slices underwent a baking process at 60°C for a duration of 12 hours. Subsequently, the slices were subjected to a dewaxing procedure: initially, they were immersed in xylene for three cycles of 20 minutes each. Following this, the slices were sequentially exposed to ethanol concentrations of 100%, 100%, 95%, 85%, and 75%, with each concentration maintained for 5 minutes. Finally, the slices were thoroughly rinsed with distilled water for a period of 5 minutes. The hematoxylin stain was applied for a duration ranging from 1 to 10 minutes, followed by a thorough rinse with distilled water. Subsequently, the blue color was restored by treating the sample with PBS. As for eosin staining, it was performed for a period of 1 to 5 minutes, after which the sample was rinsed with distilled water. The slices underwent two cycles of immersion in xylene for a duration of 10 minutes each. Ultimately, the slices were carefully sealed with neutral gum and subjected to microscopic observation.

Bioinformatics analysis

The Biostatistics analysis was conducted using R version 4.3.0, employing a two-sided test. The Mann-Whitney U test was utilized for comparisons between the two groups. Pearson's correlation test was applied for correlation analysis. AML patients were stratified into BMAL1-high and BMAL1-low mRNA expression groups using the minimum p-value method.[68] Survival analysis was performed using the Kaplan-Meier method and the log-rank test. $p < 0.05$ was set as statistically significant.

QUANTIFICATION AND STATISTICAL ANALYSIS

Data were presented as mean ± SD. The data underwent a Shapiro-Wilk normality test prior to analysis. For normally distributed data, unpaired two-tailed t-tests were used for comparisons between two groups, while one-way or two-way ANOVA followed by post hoc Dunnett, Tukey, or Šídák test were employed for comparisons involving three or more groups. Non-normally distributed data were analyzed using non-parametric tests, with the Mann-Whitney U test for comparisons between two groups and the Kruskal-Wallis test followed by the Dunn post hoc test for analyses involving three or more groups. Survival analysis was conducted using the log-rank test, and correlation analysis was performed using Spearman's rank correlation. All statistical analyses were performed using Prism 9.0 (GraphPad). For all graphs: ns: $p > 0.05$; *, $p < 0.05$; **: $p < 0.01$, ***: $p < 0.001$, ****: $p < 0.0001$.